Self-aggregation of convection in long channel geometry

Allison A. Wing [a*], Timothy W. Cronin [b]

[a]*Lamont-Doherty Earth Observatory, Columbia University, PO Box 1000, Palisades, NY 10960*

[b]*Department of Earth and Planetary Science, Harvard University, 20 Oxford St., Cambridge, MA 02138.*

[*]Correspondence to: Allison A. Wing, Lamont-Doherty Earth Observatory, Columbia University, PO Box 1000, Palisades, NY 10960, USA.

Cloud cover and relative humidity in the tropics are strongly influenced by organized atmospheric convection, which occurs across a range of spatial and temporal scales. One mode of organization that is found in idealized numerical modeling simulations is self-aggregation, a spontaneous transition from randomly distributed convection to organized convection despite homogeneous boundary conditions. We explore the influence of domain geometry on the mechanisms, growth rates, and length scales of self-aggregation of tropical convection. We simulate radiative-convective equilibrium with the System for Atmospheric Modeling (SAM), in a non-rotating, highly-elongated 3D channel domain of length $> 10^4$ km, with interactive radiation and surface fluxes and fixed sea-surface temperature varying from 280 K to 310 K. Convection self-aggregates into multiple moist and dry bands across this full range of temperatures. As convection aggregates, we find a decrease in upper-tropospheric cloud fraction, but an increase in lower-tropospheric cloud fraction; this sensitivity of clouds to aggregation agrees with observations in the upper troposphere, but not in the lower troposphere. An advantage of the channel geometry is that a separation distance between convectively active regions can be defined; we present a theory for this distance based on boundary layer remoistening. We find that surface fluxes and radiative heating act as positive feedbacks, favoring self-aggregation, but advection of moist static energy acts as a negative feedback, opposing self-aggregation, for nearly all temperatures and times. Early in the process of self-aggregation, surface fluxes are a positive feedback at all temperatures, shortwave radiation is a strong positive feedback at low surface temperatures but weakens at higher temperatures, and longwave radiation is a negative feedback at low temperatures but becomes a positive feedback for temperatures greater than 295-300 K. Clouds contribute strongly to the radiative feedbacks, especially at low temperatures.

1. Introduction

Tropical clouds and relative humidity play a key role in both the planetary energy balance and the sensitivity of global climate to radiative forcing. A large fraction of tropical cloudiness and rainfall (approximately 50% (Nesbitt *et al.* 2000; Tan *et al.* 2013)) is associated with organized convection, and recent work suggests that the frequency of organized convection in the tropics is increasing with warming (Tan *et al.* 2015). It has been recently suggested that some modes of convective organization may result from an instability of the background state of radiative-convective equilibrium, which results in separation of the atmosphere into moist regions with ascent and dry regions with subsidence (Emanuel *et al.* 2014). If such an instability indeed exists in the real atmosphere, it would reshape our understanding of tropical circulations, and could help to explain the growth and life cycle of large-scale organized convective systems such as tropical cyclones and the Madden-Julian Oscillation (e.g., Bretherton *et al.* 2005; Sobel and Maloney 2012). If this instability is temperature-dependent, as suggested by numerical modeling studies (Khairoutdinov and Emanuel 2010; Wing and Emanuel 2014; Emanuel *et al.* 2014), then the increasing tendency of convection to organize with warming could also alter the climate sensitivity significantly (Khairoutdinov and Emanuel 2010); it is unclear whether current global climate models capture this process adequately.

In this paper, we use self-aggregation to mean the spontaneous transition in a model from a state of homogenous convection and rainfall, to a state of heterogeneous convection and rainfall, with homogeneous boundary conditions. With this definition, self-aggregation is widespread in numerical models of the atmosphere that are forced with spatially homogeneous sea-surface temperatures and insolation. Self-aggregation occurs in models with high resolution and varied geometry, from 2D (Held *et al.* 1993; Grabowski and Moncrieff 2001, 2002; Stephens *et al.* 2008), to small-domain square 3D (Tompkins and Craig 1998; Bretherton *et al.* 2005; Muller and Held 2012; Jeevanjee and Romps 2013; Wing and Emanuel 2014), to elongated channel 3D (Posselt *et al.* 2008; Stephens *et al.* 2008; Posselt *et al.* 2012), as well as regional or global models with parameterized clouds and convection (Su *et al.* 2000; Held *et al.* 2007; Popke *et al.* 2013; Becker and Stevens 2014; Reed *et al.* 2015). The spontaneous symmetry-breaking suggested by the 2-dimensional latitude-height study of Raymond (2000) and by the 2-column model of Nilsson and Emanuel (1999), as well as the existence of multiple equilibria in single-column (Sobel *et al.* 2007) and 2D cloud resolving (Sessions *et al.* 2010) simulations employing the weak temperature gradient approximation, may also be interpreted as falling under this broad definition of self-aggregation of convection. There is also observational evidence for the dependence of the area-average atmospheric state on the degree of aggregation of convection that is in some ways consistent with numerical simulations (Tobin *et al.* 2012, 2013).

Is the phenomenon of self-aggregation in a 200 km $\times$ 200 km domain in a model with explicit convection and clouds possibly the same as that in a 20000 km $\times$ 20000 km domain in a model with parameterized convection and clouds? This question has largely gone unaddressed, but it is essential to answer if we want to understand the robustness of self-aggregation across our modeling hierarchy and its relevance to the real atmosphere. We seek to address this question by focusing on the following three goals:

1. To investigate the details of self-aggregation across temperatures in long channel geometry by quantifying its growth rates, physical mechanisms, and length scales
2. To compare these findings to previous results in square geometry and available observations
3. To propose a theory for the length scale of self-aggregation based on the temperature dependence of the size of multiple moist and dry bands that develop in channel geometry.

Non-rotating simulations of square domains with side lengths less than 1000 km form the bulk of the body of previous work on self-aggregation, but they have given at most one convectively active region within the domain, and have thus failed to identify any length scales of self-aggregation that differ from the limits imposed by the domain. This is disconcerting because the growth rates and length scales of dynamical instabilities are generally interrelated, so the suppression of wavelengths larger than the domain size may also artificially truncate unstable modes that could exist in the real tropical atmosphere. To avoid these

problems, we use a long channel setup similar to Posselt *et al.* (2008), which allows aggregation to occur across a much broader range of length scales than in square geometry.

Previous studies of self-aggregation are briefly reviewed in Section 2. Section 3 describes our model setup, and Section 4 presents basic results. We describe our analysis framework and apply it to the model results in section 5. Section 6 introduces a simple model for a remoistening length scale relevant for aggregation, and section 7 places our results in the context of previous studies, emphasizing comparison to square geometry. The paper concludes with a summary in Section 8.

2. Literature Review

In cloud-resolving simulations of radiative-convective equilibrium (RCE) over square 3D domains, with side lengths being hundreds of kilometers, self-aggregation has usually manifested as a single intensely precipitating cluster, surrounded by dry, subsiding air. Bretherton *et al.* (2005) and Muller and Held (2012) argued that convection–moisture–radiation feedbacks, which dry the drier air columns and moisten the moister air columns, are critical for self-aggregation; Wing and Emanuel (2014) clarified that clear-sky longwave radiation and wind-driven surface flux feedbacks dominate the early stages of aggregation. But our understanding of self-aggregation based on these results from square 3D domains has been complicated by the sensitivity of the existence of aggregation to domain size, horizontal resolution, and temperature (Muller and Held 2012; Jeevanjee and Romps 2013; Wing and Emanuel 2014). As reviewed below, self-aggregation may be more robust when model configurations are employed that include at least one side length $\mathcal{O}(10^4)$ km.

In the small (640 km) cloud-resolving 2D simulations of Held *et al.* (1993), convection aggregated only when x-averaged winds were constrained to vanish, and could be destroyed by a small amount of vertical wind shear. Grabowski and Moncrieff (2001) also found self-aggregation in a much larger (20,000 km) 2D domain, at multiple scales and into multiple clusters. Large-scale aggregation occurred despite fixed radiative cooling and was attributed to convective momentum transport and its effects on surface processes. Grabowski and Moncrieff (2002) found that interactive radiation increased the strength of aggregation, as quantified by the spatial variance of precipitable water, and caused the larger envelope of convection to follow the mean flow; aggregation was not destroyed by vertical wind shear, but its characteristics were altered.

A small number of studies have simulated self-aggregation in elongated 3D channel geometry with cloud-resolving models, which allows for both large scale overturning circulations and 3D turbulence at the scale of individual convective cells. Stephens *et al.* (2008), Posselt *et al.* (2008), and Posselt *et al.* (2012) all analyzed 3D channel simulations with a cloud resolving model over a horizontal domain of 9600 km $\times$ 180 km, and found that large regions of organized convection developed, each associated with an overturning circulation and separated by regions of clear air. The distinct dry and moist regions remained coherent and stationary in time, and grew to $\mathcal{O}(1000)$ km in size, roughly half as large as in the complementary 2D simulations of Stephens *et al.* (2008).

In addition to the self-aggregation observed in cloud resolving simulations, forms of self-aggregation have also been found in RCE simulations using regional or global models with parameterized clouds and convection. Su *et al.* (2000) found that large cloud clusters developed spontaneously in a regional model despite horizontally homogeneous boundary conditions and forcing, but only when domain-mean ascent with a peak in the upper troposphere was prescribed. General circulation models (GCMs) have been used to simulate non-rotating, global RCE with initially homogeneous surface boundary conditions and uniform insolation (Held *et al.* 2007; Popke *et al.* 2013; Becker and Stevens 2014; Reed *et al.* 2015). The details of the surface boundary condition in these simulations differ, ranging from fixed sea-surface temperature (Held *et al.* 2007; Reed *et al.* 2015) to slab ocean (Popke *et al.* 2013; Becker and Stevens 2014; Reed *et al.* 2015) to land-like slab (Becker and Stevens 2014), but in all cases large-scale circulations develop and precipitation organizes into clusters. Although the mechanisms that lead to clustering in these simulations have not been analyzed in detail, and the spatial and temporal coherence of convection vary widely, these studies indicate that resolving convection may not be a necessary condition for self-aggregation. As noted by Held *et al.* (2007), the hypothetical state of an identical radiative-convective equilibrium

solution in many connected GCM columns with uniform forcing is likely to be unstable.

Although we do not discuss further the comparison of cloud-resolving and GCM simulations in this paper, we believe that of the above options, cloud-resolving simulations in a long 3D channel represent the best prospect for bridging between cloud-scale and planetary-scale processes.

3. Simulation Design

We simulate statistical radiative-convective equilibrium (RCE) using version 6.8.2 of the System for Atmospheric Modeling (SAM, Khairoutdinov and Randall (2003)) cloud-system-resolving model. We use a highly elongated doubly-periodic non-rotating 3D channel domain, with 4096×64 grid points in the horizontal, and a relatively coarse horizontal resolution of 3 km. The domain size is thus 12288 km × 192 km – nearly a third of the equatorial circumference in length, but less than 2 degrees wide (this setup is similar to that of Posselt *et al.* (2008), Stephens *et al.* (2008), and Posselt *et al.* (2012)). We use the variable x or the terms "length" or "along-channel" to refer to distance parallel to the 12288-km axis of the channel, and the variable y or the terms "width" or "cross-channel" to refer to distance perpendicular to the 12288-km axis of the channel. The channel width of 192 km permits multiple convective cores in the cross-channel direction, and for cold pools that spread in both the x- and y-directions. We impose no background flow, but we do not constrain mean winds to vanish either, so weak (<10 m s^{-1}, with amplitude peak in the lower stratosphere) domain-mean sheared flows develop. These flows are reminiscent of the quasi-biennial oscillation (as in Held *et al.* 1993; Yoden *et al.* 2014), but have a much shorter period (tens of days). We use the SAM 1-moment microphysics parameterization and, for the main set of simulations, the radiation code from the National Center for Atmospheric Research (NCAR) Community Atmosphere Model version 3 (CAM, Collins *et al.* 2006), with CO_2 mixing ratio fixed at 355 ppm. As a sensitivity test, we perform several additional simulations with an alternate radiation scheme, the Rapid Radiative Transfer Model (RRTM, Mlawer *et al.* 1997; Clough *et al.* 2005; Iacono *et al.* 2008).

The lower boundary is a sea surface of uniform temperature T_S, varying across simulations from 280 K to 310 K (a much wider range than the 298 K to 302 K of Posselt *et al.* (2012)). The upper boundary is a rigid lid at 28 km, with a sponge layer extending from 19 km to 28 km; the vertical grid has 64 levels and variable spacing, with 8 levels in the lowest km and 500 m spacing above 3 km. Solar forcing is specified as an equinoctial (julian day 80.5) diurnal cycle of insolation at 19.45° N latitude, with a time-mean insolation of 413.6 W m^{-2}. This representative diurnal cycle is chosen to match the annual-mean insolation on the equator, and gives an insolation-weighted cosine zenith angle of 0.74, comparable to the value of 0.744 for a point on the equator when averaging over both seasonal and annual cycles (Cronin 2014).

Each simulation is run for 75 days following initialization with an average sounding from the final 20 days of a 100-day simulation of RCE with the same boundary conditions, but a much smaller domain, 64×64 grid cells in the horizontal. A small amount of thermal noise is added to the five lowest layers (an amplitude of 0.1 K in the lowest layer, decreasing linearly to 0.02 K in the fifth layer), allowing convection to start within the first few hours of each simulation.

A useful metric across temperatures is the column relative humidity or saturation fraction, $\mathcal{H}$, which is the ratio of the precipitable water $\widehat{q}$ to the saturation water vapor path $\widehat{q^*}$ (e.g., Bretherton *et al.* 2005). We denote the density-weighted vertical integral of a variable over the full depth of the simulated atmosphere ($z = [0, z_t]$) with an overhat $\widehat{(\cdot)}$, the horizontal mean of a quantity with angle brackets $\langle(\cdot)\rangle$, and q and q^* represent the actual and saturation mixing ratios of water vapor (see Appendix A for a brief list of notation conventions). We define the saturation mixing ratio q^* as that over ice below 253.15 K, that over liquid above 273.15 K, and a weighted average of the two between those temperatures, consistent with the thermodynamics of SAM (Khairoutdinov and Randall 2003). We have hourly output for $\widehat{q}$ at each grid point, but infrequent 3D output limits our ability to accurately calculate $\widehat{q^*}$ on an hourly basis at each grid point over both water and ice, so we use a value of $\widehat{q^*}$ based on the hourly values of the domain-average temperature profile ($\langle T\rangle$) :

$$\mathcal{H} = \frac{\widehat{q}}{\widehat{q^*(\langle T\rangle)}}. \quad (1)$$

We use $\mathcal{H}$ as a measure of convective aggregation because it varies little with absolute temperature (always taking values between 0 and 1), it integrates the effects of vertical motion over time, and it acts as an active tracer by influencing convection, cloud formation, and clear-sky radiative heating.

4. Results

Hovmuller plots of the y-averaged column relative humidity $\mathcal{H}$ (Equation 1) reveal self-aggregation across the full range of T_S, from 280 K to 310 K (Figure 1). At each value of T_S, a state with initially homogeneous $\mathcal{H}$ spontaneously separates into a state with banded moist and dry regions, and the size of the banded regions grows in time, though not indefinitely. Posselt *et al.* (2012) similarly depict aggregation in their 3D channel simulations, and most of the features they discuss are also found in our simulations, as described below.

As an example, we consider the simulation at 305 K (Figure 1f), where the atmosphere initially has uniform $\mathcal{H}$=0.742. The evolution of aggregation in this simulation, including the cross-channel variability, is shown in Video S1. Within the first few days of the simulation, dry and moist anomalies begin to develop, and disturbances propagate along the channel in both directions with typical propagation speeds of $\sim$20 m s^{-1}. Inspection of x-z cross sections (not shown) suggests that these disturbances are consistent with second baroclinic mode convectively coupled gravity waves, which have lower-tropospheric descent and upper-tropospheric ascent in regions with active convection. By day 15, several nearly stationary dry regions emerge; these regions (as well as others that newly appear) expand and become drier from about day 15 to about day 40. Interspersed between these dry regions are anomalously moist regions, as well as propagating disturbances, which appear as moist and dry anomalies themselves and also modulate the intensity and size of the nearly stationary moist and dry regions. By day 50, there are three large dry regions that have particularly low values of column relative humidity ($\mathcal{H} \approx$ 0.22-0.3), centered near 3500 km, 5500 km, and 7200 km. Multiple other smaller and weaker dry regions are found elsewhere in the domain. There are also instances of dry regions merging; for example, two narrow dry regions between 0 and 1000 km merge to form a single larger dry region (with lower $\mathcal{H}$) between days 50 and 60. From days 50 to 75, the simulation reaches a dynamic balance on the domain-scale between creation of new dry regions and destruction of existing ones, with about 8-10 convectively active moist regions, and a similar number of convectively suppressed dry ones. But substantial variability remains; in particular, the location of moist and dry regions oscillates back and forth with time, with a period of about 6-7 days. This oscillation of the location of moist and dry regions appears to be related to variations in the strength of the convectively active regions, which are often in phase nearby, but out of phase at larger distances; we speculate that this oscillation is related to the time it takes for a 2nd- or 3rd- mode convectively coupled gravity wave to propagate along the length of the domain back to its starting point. By the end of the simulation – averaging over days 50-75 – the domain-mean $\mathcal{H}$ falls to 0.581, and the spatial standard deviation of $\mathcal{H}$ rises to 0.13; self-aggregation increases the spatial variance of humidity, and dries the domain as a whole.

The details of this picture – propagation speed of initial disturbances, timing of development of dry regions, and timing and location of mergers of anomalously dry regions – vary across simulations. The length scale of self-aggregation also varies systematically with temperature, and this will be discussed in more detail in subsequent sections. But the broad picture of convective self-aggregation, including the time scales, the variability of $\mathcal{H}$ in the mature state, and the general finding that aggregation warms and dries the troposphere, are relatively insensitive to mean temperature. Domain-average summary statistics for the set of simulations across T_s are shown in Table 1.

In all simulations, the troposphere warms and dries relative to the initial condition (Figure 2(a)), though the stratosphere cools in simulations where T_S is lower than 300 K (Figure 2(b); Table 1). Tropospheric warming overall, and the increase in tropospheric warming with T_S, are consistent with the finding by Singh and O'Gorman (2013) that the lapse rate in RCE depends on entrainment and free-tropospheric relative humidity. In our simulations, aggregation decreases the free-tropospheric relative humidity in the domain mean, but increases the free-tropospheric relative humidity in convectively active regions, plausibly reducing the influence of entrainment on the lapse rate

and driving the thermal structure of the troposphere closer to a moist adiabat. Warming of the troposphere with aggregation can also be explained as a consequence of convective cores in moist regions drawing air with higher moist static energy from deeper within the boundary layer (Held *et al.* 1993).

The horizontal mean relative humidity decreases in all simulations at nearly all heights as a consequence of self-aggregation, with peak drying by ∼0.3 near 700 hPa at all temperatures, and a secondary peak in the drying near the upper tropospheric peak in warming (Figure 2(c)). The simulations with higher T_S tend to dry slightly more, although the simulations at 295 K and 300 K are exceptions to this monotonicity. The mean outgoing longwave radiation increases over the course of each simulation as a consequence of this drying, by an amount that increases with T_S, ranging from ∼11 W m^{-2} at 280 K to ∼24 W m^{-2} at 310 K (Table 1).

5. Analysis

5.1. *Moist Static Energy Variance Budget*

As shown above, self-aggregation is characterized by the amplification and expansion of dry anomalies. To quantify the growth rates and physical mechanisms of this evolution, we use a variance budget of vertically-integrated frozen moist static energy, following Wing and Emanuel (2014). This framework enables the quantification of the processes that lead to growth or decay of anomalies of vertically-integrated frozen moist static energy from its spatial mean. The frozen moist static energy (hereafter referred to as h) is conserved in dry and moist adiabatic displacements, as well as freezing and melting of precipitation; h is given by the sum of the internal energy, c_pT, the gravitational energy, gz, and the latent energy, $L_vq - L_fq_{c,i}$ (c_p is the specific heat of dry air at constant pressure and g is the gravitational acceleration). In the latent energy term, L_v is the latent heat of vaporization, q is the water vapor mixing ratio, L_f is the latent heat of fusion, and $q_{c,i}$ is the condensed ice water mixing ratio:

$$h = c_pT + gz + L_vq - L_fq_{c,i}. \tag{2}$$

Because h is conserved in moist adiabatic processes, its density-weighted vertical integral, $\widehat{h}$, is conserved under vertical convective mixing.

If weak temperature gradients can be assumed in the free troposphere (Sobel *et al.* 2001), then spatial variance in $\widehat{h}$ is dominated by variance in $L_v\widehat{q}$ rather than $c_p\widehat{T}$. Amplification of moist or dry anomalies can occur adiabatically – by advection alone – or diabatically – by processes that lead to anomalous heating or moistening of moist columns or to anomalous cooling or drying of dry columns. Atmospheric heating and cooling lead, respectively, to moistening and drying, because the weak temperature gradient approximation implies that anomalous heating is largely balanced by ascent, converging moisture into the column, while anomalous cooling is largely balanced by descent, diverging moisture out of the column.

We use the budget equation for the evolution of $\widehat{h'}^2$, the squared anomaly of $\widehat{h}$ from its spatial mean (derived in Wing and Emanuel 2014):

$$\frac{1}{2}\frac{d\widehat{h'}^2}{dt} = \widehat{h}'F_K' + \widehat{h}'N_S' + \widehat{h}'N_L' - \widehat{h}'\nabla_h \cdot \widehat{\mathbf{u}h}, \tag{3}$$

where F_K is the surface enthalpy flux, N_S is the column shortwave flux convergence, N_L is the column longwave flux convergence, and $-\nabla_h \cdot \widehat{\mathbf{u}h}$ is the horizontal convergence of the density-weighted vertical integral of the flux of frozen moist static energy. We refer to $-\widehat{h}'\nabla_h \cdot \widehat{\mathbf{u}h}$ as the advective term, and we calculate it as a residual from the rest of the budget. A primed quantity, $(\cdot)'$, denotes the spatial anomaly from the horizontal mean, $\langle(\cdot)\rangle$. Equation (3) decomposes the growth or decay of $\widehat{h'}^2$ into an advective term, as well as three diabatic components, associated with the correlation of anomalous column-integrated frozen moist static energy with anomalous surface enthalpy fluxes, shortwave atmospheric heating, or longwave atmospheric heating. The fluxes F_K, N_S, and N_L are defined such that positive anomalies in each indicate anomalous sources of energy for the column. Note that each term on the right hand side of (3) is a feedback with regard to the energy budget of the atmospheric column and not the atmosphere-surface system. For example, "positive longwave radiative feedback" indicates there is less cooling of the atmosphere itself in moist regions (where $\widehat{h}' > 0$),

rather than less outgoing radiation at the top of the atmosphere. This is an important distinction because moistening always leads to less top-of-atmosphere longwave cooling, but does not always lead to less atmospheric longwave cooling. A positive feedback is one that causes $\widehat{h'}^2$ to increase, and indicates that the associated physical mechanism furthers aggregation.

The budget of $\widehat{h'}^2$ can be examined locally, or in a spatially-integrated sense across the whole domain. Because the units of $\widehat{h'}^2$ are not particularly intuitive, and magnitudes of $\widehat{h'}^2$ vary considerably in time, we normalize equation (3) by the domain-mean variance $\langle \widehat{h'}^2 \rangle \equiv \mathrm{var}(\widehat{h})$, which itself evolves in time. Taking the spatial average over the whole domain gives:

$$\frac{d\ln\left[\mathrm{var}(\widehat{h})\right]}{dt} = \frac{2\langle \widehat{h'} F'_K \rangle}{\mathrm{var}(\widehat{h})} + \frac{2\langle \widehat{h'} N'_S \rangle}{\mathrm{var}(\widehat{h})} + \frac{2\langle \widehat{h'} N'_L \rangle}{\mathrm{var}(\widehat{h})} - \frac{2\langle \widehat{h'} \nabla_h \cdot \widehat{\mathbf{u}h} \rangle}{\mathrm{var}(\widehat{h})}. \tag{4}$$

With this normalization, the left hand side gives the full relative growth (or decay) rate of $\mathrm{var}(\widehat{h})$, and the right hand side decomposes this growth rate into four components each associated with a physical mechanism; each term has units of inverse time, expressed in plots as day^{-1}.

5.2. *Growth Rates*

Because the instability of the channel simulations to convective organization ultimately results in a statistically stable state, it makes sense to think about the instability as a problem of logistic growth, rather than pure exponential growth. The increase of variance of $\widehat{h}$ then follows:

$$\frac{d}{dt}\mathrm{var}(\widehat{h}) = \frac{1}{\tau}\mathrm{var}(\widehat{h})\left[1 - \frac{\mathrm{var}(\widehat{h})}{K_{\widehat{h}}}\right], \tag{5}$$

where τ is the exponential growth time scale of the small-amplitude linear instability, and $K_{\widehat{h}}$ is the maximum column-integrated frozen moist static energy variance, which occurs in the aggregated state.

The evolution of the domain-mean column frozen moist static energy variance, $\mathrm{var}(\widehat{h})$, is shown in Figure 3(a), as are fits of the logistic growth equation. In each simulation, $\mathrm{var}(\widehat{h})$ increases rapidly (over an order of magnitude) within the first 10-20 days, before leveling off. The rate of increase slows earlier at low T_S than at higher T_S. The magnitude of the increase in $\mathrm{var}(\widehat{h})$ increases with T_S; in the coldest simulation (T_S=280 K), it increases by about an order of magnitude, whereas in the warmest simulation (T_S=310 K), it increases by about two orders of magnitude. The value of $\mathrm{var}(\widehat{h})$ in the steady state also is larger in the warmer simulations. When we instead consider the evolution of the domain-mean column relative humidity variance, $\mathrm{var}(\mathcal{H})$, the final value attained varies by less than an order of magnitude across the range of T_S (Figure 3(b)). The average of $\mathrm{var}(\mathcal{H})$ over days 50-75 of the simulation ranges from 0.015 to 0.027 but does not vary systematically with temperature (Table 1). Note that the scale for spatial variation in $\mathcal{H}$ is $[\mathrm{var}(\mathcal{H})]^{1/2}$, so $\mathrm{var}(\mathcal{H})\sim 0.02$ corresponds to typical deviations of column relative humidity from the domain mean of $\sim$14%.

Logistic growth fits to either $\mathrm{var}(\mathcal{H})$ or $\mathrm{var}(\widehat{h})$ give an exponential growth time scale, τ, between 2 and 6 days (Figure 3, Table 1). Thus, growth time scales here are shorter than those in the square domain simulations of Bretherton *et al.* (2005) ($\sim$ 9 days) and Wing (2014) ($\sim$10-12 days). The cause of these differences, and what sets the general time scale of self-aggregation, remains an open question and will not be further addressed in this paper.

5.3. *Physical Mechanisms*

Using the budget equation (4) for $\mathrm{var}(\widehat{h})$ we first consider the mechanisms that dominate the initial stages of self-aggregation – the first 10-20 days. In this initial period, the diabatic contributions from radiation and surface fluxes – the first three terms on the right hand side of (4) – act to increase $\mathrm{var}(\widehat{h})$, while the advective term acts to decrease $\mathrm{var}(\widehat{h})$ (Figure 4). The partitioning of the diabatic contributions, however, varies with surface temperature. In all simulations, feedbacks involving shortwave radiation and surface fluxes amplify anomalies in $\widehat{h}$. In the four coldest simulations, (T_S = 280K, 285K, 290K, 295K), the longwave radiation is at first a negative feedback, but in the warmer simulations, it is an important positive feedback. The magnitude of the shortwave feedback decreases by nearly a factor of 10 as the surface temperature increases from 280 K to 310 K, and the shortwave feedback also becomes much less important relative to the other feedbacks; we discuss reasons for this below (Section 7.3). The

magnitude and relative importance of the surface flux feedback is similar across simulations at different T_S.

The contribution of all three diabatic processes to the initial growth of $\mathrm{var}(\widehat{h})$ resembles previous work (Wing and Emanuel 2014), but the role of the advective term differs, especially later in the simulation, because in the simulations reported here the advective term always acts to decrease $\mathrm{var}(\widehat{h})$, opposing aggregation. Put another way, the bulk circulation always has positive gross moist stability, and never transports moist static energy upgradient. This finding holds for all temperatures, with the possible exception of the warmest simulation, where T_S = 310K, in which the advective term oscillates about zero in the second half the simulation (Figure 4(g)).

As in previous work (Muller and Held 2012; Wing and Emanuel 2014), we find that processes can differ in their relative contributions to initial growth and maintenance of the aggregated state. For example, the surface flux term is much more important for the initial growth of $\mathrm{var}(\widehat{h})$ than for the maintenance of $\mathrm{var}(\widehat{h})$. In all but the two coldest simulations (T_S = 280K, 285K), the surface flux feedback is the largest contributor to the initial growth of $\mathrm{var}(\widehat{h})$ (Figure 4(c)-(g)). By day 10-30 (depending on the simulation), however, the surface flux feedback becomes negligible, or even negative. The declining importance of the surface flux feedback with time results from competing effects of variations in the surface wind speed and air-sea enthalpy disequilibrium effects; however, the surface flux feedback remains positive longer in our channel simulations than it did in the square simulations of Wing and Emanuel (2014), at least relative to when an equilibrium state is reached.

Shortwave and longwave radiation contribute to both growth and maintenance of $\mathrm{var}(\widehat{h})$. The shortwave feedback term is positive, and remarkably constant in time after the the first few days. In the four coldest simulations, once the longwave feedback switches from negative to positive, it remains positive for the remainder of the simulation; it is also positive throughout in the simulation at 300K (Figure 4(a)-(e)). In the two warmest simulations (T_S = 305K, 310K), the longwave feedback term is near zero at the end of the simulation (Figure 4(f),(g)). Even though the longwave feedback is zero in the domain mean, it nonetheless contributes significantly to maintaining the $\widehat{h}$ anomalies in the moist regions (not shown).

The radiative feedbacks can be further decomposed into the contributions to radiative transfer from clear-sky and clouds, by calculating the second and third terms on the right hand side of (4), $\frac{2\langle \widehat{h}' N_S' \rangle}{\mathrm{var}(\widehat{h})}$ and $\frac{2\langle \widehat{h}' N_L' \rangle}{\mathrm{var}(\widehat{h})}$, using the clear-sky radiative fluxes and comparing to the all-sky fluxes (Figure 5). This decomposition reveals that the positive shortwave feedback in the initial stages of aggregation is predominantly a cloud effect, especially in the colder simulations. The fraction of the domain-mean shortwave feedback contributed by the clear-sky fluxes during the rest of the simulation increases from 29% to 79% as T_S increases from 280 K to 310 K (Table 2). The negative longwave feedback in the first few days of the four coldest simulations is also a result of clouds; the clear-sky longwave feedback term is nearly zero and not strongly negative at that time. The contribution of clear-sky processes to the total longwave feedback during the rest of the simulation varies with T_S; in the two coldest simulations (T_S = 280 K, 285 K), the magnitude of the clear sky longwave feedback is about half of the total (positive) longwave feedback. In the other simulations the clear-sky longwave feedback is near zero or negative while the total longwave feedback is positive or near zero.

Since self-aggregation begins as an amplification of a dry region (Wing and Emanuel 2014), decomposing the initially positive longwave feedback in the driest regions may help to more deeply understand the role of clouds in aggregation. The fraction of the positive total longwave feedback that is contributed by the clear-sky fluxes in the driest 10% of the domain in the beginning of the simulation is between 24% and 49% for all simulations except the coldest (T_S = 280K), for which the clear sky term contributes 86% (Table 2). This percentage was determined by taking an average over the days in which there is a positive longwave feedback in the dry region. The consistency of this result with previous work will be discussed below (Section 7.2).

Overall, surface flux feedbacks contribute strongly to the initial instability in all simulations, longwave radiative feedbacks contribute strongly in the warmer simulations, and shortwave cloud radiative feedbacks contribute strongly in the colder

simulations. Advection of moist static energy by the circulation nearly always opposes self-aggregation.

5.4. *Length Scales*

In order for the domain as a whole to reach a steady state, the time tendency of $\mathrm{var}(\widehat{h})$ must approach zero, and the length scales of convective aggregation must also approach statistical stationarity. For each hour of output data, we quantify the length scales associated with convective aggregation by analyzing the power spectrum, $\phi(k)$, of the y-averaged precipitable water, $\widehat{q(x)}$:

$$\phi(k) = \left| \int_0^{L_x} \widehat{q(x)} \exp\left(\frac{2\pi i k x}{L_x}\right) dx \right|^2, \tag{6}$$

where L_x is the length of the channel in the long direction, and k is the wavenumber (in cycles per channel length). We use two metrics of dominant length scales: one is based on the autocorrelation length, and the other is based on the power-weighted average wavenumber of spatial variability of precipitable water.

The autocorrelation function is given by the inverse Fourier transform of the power spectrum ϕ, and the autocorrelation length L_{cor} is the distance at which the autocorrelation function decays to $1/e$ of its maximum value (this is the measure of autocorrelation length scale used in Craig and Mack (2013)). For a perfectly sinusoidal variable, the wavelength λ is related to L_{cor} by $\lambda = 2\pi[\arccos(e^{-1})]^{-1} L_{cor} \approx 5.26 L_{cor}$; thus, to calculate a length scale representative of the full wavelength of a disturbance, we use the value of L_{cor} scaled by this factor.

The second metric, $L_{\{k\}}$, is given by simply dividing the channel length, L_x, by the power-weighted average wavenumber of spatial variability of precipitable water, $\{k\}$:

$$\{k\} = \frac{\sum_{k=1}^{k_{nyq}} k\phi(k)}{\sum_{k=1}^{k_{nyq}} \phi(k)}, \tag{7}$$

$$L_{\{k\}} = L_x / \{k\} \tag{8}$$

where k_{nyq} is the Nyquist wavenumber, or $[L_x/(2\Delta x) - 1]$, and Δx is the grid spacing in the horizontal. This second metric, $L_{\{k\}}$, weights higher wavenumbers more strongly than the correlation length metric, $5.26 L_{cor}$, because the calculation of $\{k\}$ does not account for the lack of coherence of spectral power at higher wavenumbers. Failure to account for coherence is in some ways a flaw of the second method; however, the threshold definition of L_{cor}, as the $1/e$-crossing of the autocorrelation function, can lead to abrupt changes of L_{cor} in time when very low wavenumbers (i.e., 1 or 2) have a significant amount of power. Thus, we present time-mean values for both $5.26 L_{cor}$ and $L_{\{k\}}$ in Table 1, but we only show values of the latter in plots.

Figure 1 shows that for all temperatures, not only do dry regions grow drier in time, but they also grow in size. The dry regions, however, do not grow in size indefinitely, nor do they all merge into one dry region and constrain convection to occur in only one moist cluster. The evolution of the length scale associated with convective organization, using the average wavenumber metric, $L_{\{k\}}$, is shown in Figure 6(a). The length scale increases, from 0 km at time t=0, to $\mathcal{O}(1000)$ km over the course of each simulation, and also tends to decrease with increasing T_S. The mean of $L_{\{k\}}$ over the last 25 days of each simulation, $\overline{L_{\{k\}}}^{d50:75}$, decreases from 2252 km in the simulation at 280 K to 1027 km in the simulation at 310 K (Table 1), although the 290 K simulation is an outlier to the otherwise monotonic relationship. An alternative metric of the length scale of aggregation, the autocorrelation length, also indicates that the scale decreases with temperature (Table 1). Although the length scales do not increase indefinitely, they exhibit significant variability throughout each simulation, particularly at lower surface temperatures (Figure 6(a)); timeseries of both metrics together (not shown) indicate that temporal variability of $5.26 L_{cor}$ closely follows that of $L_{\{k\}}$.

The power spectrum $\phi(k)$ (Figure 6(b)) generally has largest values at low wavenumbers, with a peak for some $k < 10$, then a transition to roughly k^{-3} decay for $10 < k < 1000$, and a flattening out for $k > 1000$, where variability on the scale of convective cores becomes important. The spectral slope is not exactly $\sim k^{-3}$ (it steepens with temperature), and it is an open question whether this value is at all related to other k^{-3} slopes in turbulence theory. There does appear to be somewhat of a qualitative shift at the lowest sea-surface temperatures, 280 K and 285 K, where there is roughly an order of magnitude more power for very low wavenumbers k=1-3 than for k$\lesssim$10. These

low temperatures still have a flat spectrum out to $k \sim 10$, though, which leads to the largest discrepancy between the length scale metrics $L_{\{k\}}$ and $5.26L_{cor}$; $\overline{5.26L_{cor}}^{d50:75}$ rises to over 4000 km for both 280 K and 285 K, which is more than double the value of $\overline{L_{\{k\}}}^{d50:75}$. Simulations with an even longer channel might be required to obtain cleaner statistics for the correlation length at the lowest temperatures.

Craig and Mack (2013) suggested that self-aggregation could be viewed as a "coarsening" process analogous to phase separation of a bistable system where the two phases are subject to diffusive mixing. They developed a simple physically-motivated model of how moisture-convection feedbacks could lead to bistability of the tropical atmosphere, and showed that this model exhibits a key indicator of coarsening: self-similar growth. Self-similarity was shown by power law growth of the autocorrelation length scale of precipitable water – $L_{cor} \sim t^b$, with an exponent $b = 1/2$ for diffusive mixing. In our simulations, plotting L_{cor} against t on log-log axes for days 1 to 10 does suggest power-law growth, with $b \approx 1$, but decreasing at the largest T_S to $b \approx 0.8$. This near-linear growth across temperatures is also evident in the overlap of all of the curves for $L_{\{k\}}$ in Figure 6(a) from days 1-5. But it is challenging to precisely determine the exponent of this initial upscale growth, because of the several hour time scale it takes for convection to start in an atmosphere initially near rest, and the variability of L_{cor}; averaging multiple runs with slightly different initial conditions (as in Craig and Mack (2013)) could help to determine whether or not b is distinguishable from 1. As noted by Craig and Mack (2013), a scale argument for $b = 1$ can be made for bistable systems where advective mixing dominates diffusive mixing (Bray 2003) – as would likely be the case here with downgradient transfer of moist static energy. In a broad sense, the self-aggregation in our simulations may be viewed as a coarsening process. However, the details differ significantly from the model of Craig and Mack (2013), both in terms of the source of mixing and the mechanisms leading to upscale growth (surface flux and radiative feedbacks instead of moisture-convection feedbacks).

6. Theory for Boundary Layer Remoistening Length Scale

The termination of the upscale growth of dry anomalies at a size much less than the length of the channel raises the question: what sets the upper limit on the size of a dry region?

Analysis of a simple model of a well-mixed boundary layer near a subsidence center and over a sea surface of uniform temperature (Appendix B) leads us to hypothesize that a boundary layer remoistening length scale, $L_M \equiv z_b/c_E$, limits the maximum size of a dry region. The remoistening length scale is the ratio of the depth of the boundary layer, z_b to a dimensionless moisture exchange coefficient, c_E, and it determines how rapidly a dry parcel of air that subsides into the boundary layer is driven back towards saturation under the combined influences of advection – both vertical and horizontal – and surface fluxes. If the boundary layer height is spatially uniform, and the top of the boundary layer sees uniform subsidence, then parcels are eventually driven towards saturation because the wind speed within the boundary layer must increase with distance from the subsidence center. These stronger winds moisten the boundary layer ever more aggressively, until the moist static energy becomes high enough to support precipitating convection. We approach the question of the upper limit to the size of a dry region, rather than the upper limit to the size of a moist region, because it does not require dealing with the dynamics of deep convection, and because previous work has shown that part of the process of self-aggregation is the expansion of dry regions; whether or not the moist regions expand with time is less clear.

Although L_M does not depend directly on temperature, the boundary layer height is an internal model parameter that decreases by about a factor of two as the surface temperature increases from 280 K to 310 K (Table 1). A decrease in the height of the well-mixed subcloud layer with increasing temperature is expected because the fractional increase in tropospheric radiative cooling with temperature is smaller than that of saturation specific humidity, so the constraint that precipitation balance tropospheric radiative cooling (e.g., Takahashi 2009) requires that the boundary layer become more humid, to slow the increase in evaporation with temperature. In our simulations, we diagnose z_b as the height of the maximum of $d^2\theta_v/dz^2$ in the unsaturated part of the

domain, using a 3-point quadratic fit so that z_b can fall between model levels. This height represents the transition in static stability at the top of the nearly-neutral subcloud layer; fitting with more points or using the height of the maximum in domain-average relative humidity alters little our estimation of z_b. The decrease in boundary layer height with warming is qualitatively similar, but noisier, if cloud fraction or cloud water content (both of which also have local maxima near the top of the boundary layer) are used to diagnose z_b. Across the set of temperatures, L_M decreases from about 640 km at 280 K to about 300 km at 310 K; the length scale of dry regions correlates with the remoistening length scale, with a best-fit line through the origin given by $L_{\{k\}} = 3.16 L_M$ (R^2=0.8, Figure 7).

This correlation is intriguing, but attempting to confirm this scaling – beyond the main set of simulations across temperatures shown here – has proven inconclusive. The boundary layer height, z_b, is difficult to directly manipulate, because it is an internal model parameter. Modifying c_E seems to be easier, but leads to changes in z_b, and in the characteristics of the aggregated state aside from mere alteration of length scales, and thus provides limited evidence for or against the theory (c_E modification simulations are described in Appendix B). A further complication is that simulations with an alternate radiation scheme (RRTM) result in reduced $L_{\{k\}}$ that no longer monotonically decreases with temperature – even though L_M is not changed much by the radiation scheme (Figure 7). These results indicate that the boundary layer remoistening length $L_M = z_b/c_E$ is unlikely to be the sole relevant length scale that determines the upper limit on the size of a dry region.

7. Discussion

7.1. *Mechanisms of Aggregation*

Using the frozen moist static energy spatial variance budget equation to characterize the physical mechanisms that lead to self-aggregation allows us to directly compare the results from our channel simulations with the results of Wing and Emanuel (2014), and qualitatively to those of other self-aggregation studies (e.g., Bretherton *et al.* 2005). Overall, the physical mechanisms of aggregation are similar: feedbacks involving longwave radiation and surface enthalpy fluxes contribute most to the initial growth in $\mathrm{var}(\widehat{h})$ and the shortwave radiation feedback is positive throughout. This results from reduced longwave cooling, enhanced shortwave heating, and enhanced surface fluxes (due to stronger winds) in the moist regions. As in this work, Bretherton *et al.* (2005) found comparable contributions from radiative and surface flux forcings to the initial growth in column relative humidity anomalies, based on fits to a semi-empirical model. It is also notable that these similarities occur despite the use of fixed solar insolation in previous studies and a diurnal cycle here. The largest difference between the physical mechanisms in our channel simulations and in the square simulations of previous studies is the role of the advective term. This term was an important positive feedback in the intermediate stages of aggregation in square simulations (Bretherton *et al.* 2005; Muller and Held 2012; Wing and Emanuel 2014), but nearly always opposes aggregation in our channel simulations. We speculate that this difference is related to the different geometries of organized convection in channel and square domains, such as the degree of symmetry and connectivity between dry and moist regions. In all of the simulations presented here, moist and dry regions remain banded for all time whereas in square simulations, aggregation begins as a circular dry patch that expands to force all convection into a circular cluster. Directly linking these topological differences to the sign of the advective term would require more detailed investigation into the structures of the circulation. Further comparison between the mechanisms of aggregation found here and previous analytical and semi-empirical models (Bretherton *et al.* 2005; Craig and Mack 2013; Emanuel *et al.* 2014) is underway but beyond the scope of this paper.

7.2. *Sensitivity to Radiation Scheme*

As noted above, in most of the channel simulations, the majority of the initial positive longwave feedback in the driest regions is a cloud effect. Previous work (Wing and Emanuel 2014; Wing 2014), however, indicated that the majority of this feedback was captured by clear sky processes, leading Emanuel *et al.* (2014) to exclude clouds from their simple two-layer model of radiative-convective instability. Because our main set of channel

simulations uses a different radiation scheme (CAM) than that of Wing and Emanuel (2014) (RRTM), this difference in the contribution of clouds to the radiative feedbacks could arise from either radiation scheme or geometry. To test which factor is more important, we repeat the 305 K square simulation configuration of Wing and Emanuel (2014), but with the CAM radiation scheme. In this sensitivity test, clouds contribute most of the initial positive longwave feedback in the driest regions, as in the channel simulations, and also in agreement with Muller and Held (2012), who used the CAM radiation scheme, and found that self-aggregation resulted from longwave cooling by low clouds. Therefore, the difference in the contribution of clouds to the radiative feedbacks seems to relate more to radiation scheme than to geometry. This sensitivity test highlights the utility of having a framework to quantify the mechanisms that contribute to self-aggregation across different model configurations.

To test whether channel geometry shows similar sensitivity to the radiation scheme, we repeat part of the main set of channel simulations, from T_S=285 K to T_S=305 K, but with the RRTM radiation scheme. Self-aggregation occurs across this range of temperatures and, in many ways, compares closely to the channel simulations described above (Sections 4-5). The physical mechanisms controlling self-aggregation are very similar, especially in terms of the initial instability, although the magnitudes of the feedback terms are about 10% smaller with RRTM than with CAM radiation. The advective term is still a negative feedback, except for the simulation with RRTM at $T_S = 300$K. Bretherton *et al.* (2005) also found that the vertical structure of the circulation, and thus the sign and strength of the advective feedback, could be sensitive to differences in the vertical profile of radiative heating due to different radiation schemes. As in the sensitivity test with square geometry above, we find that the decomposition of the radiative feedbacks between clear-sky and cloud effects depends strongly on the radiation scheme. The fractional contribution of the clear-sky shortwave feedback is 7 to 28 percentage points higher with RRTM than with CAM radiation. The fractional contribution of the clear-sky longwave feedback in the first ∼10 days of the simulation in the driest 10% of the domain is 6 to 33 percentage points higher with RRTM, except for the 295 K simulation in which it is about the same as with CAM. The growth rates of $\mathrm{var}(\widehat{h})$ are slightly slower with RRTM (∼ 4-10 days versus ∼ 2-6 days), but the significance of this is unclear. As noted in Section 5.4, the length scales of aggregation are smaller with RRTM, and do not decrease smoothly with increasing temperature as they do with CAM. Overall, clouds contribute more to the radiative feedbacks with the CAM radiation scheme than with RRTM, regardless of domain geometry. Note that it is not surprising that cloud radiative feedbacks vary with radiation scheme because different radiation schemes may assign different optical properties even to the same cloud condensate profile.

7.3. *Temperature Dependence of Aggregation*

In the elongated 3D channel simulations presented here, aggregation occurs across a wide range of temperatures (between 280 and 310 K). Previous channel simulations (Posselt *et al.* 2012) have also found aggregation to occur, but, to our knowledge, no other channel simulations have been performed at such low values of T_S. Aggregation at low temperatures (T_S = 285K) in channel geometry also occurs with the RRTM radiation scheme, so it is the domain geometry and not the radiation scheme that leads to the weaker temperature dependence of self-aggregation found in this paper. Sensitivity to domain geometry is also consistent with Wing (2014), who noted that the temperature dependence may depend on domain size. The only finding of self-aggregation at temperatures below 280 K that we are aware of is the work of Abbot (2014), where convection strongly aggregated in cloud-resolving snowball-earth tropical RCE simulations, even in very small square domains, and surface temperatures as low as ∼250 K.

The occurrence of aggregation at temperatures as low as 280 K is a striking contrast to Khairoutdinov and Emanuel (2010) and Wing and Emanuel (2014), in which aggregation in a small square domain only occurred above ∼300K. The simple two-layer model for self-aggregation presented by Emanuel *et al.* (2014) suggests that self-aggregation should be impeded by a negative clear-sky longwave feedback at low T_S, because longwave cooling of the atmosphere increases with q when the longwave opacity of the lower troposphere is low, but decreases with q when the longwave opacity of the lower troposphere is high. This latter condition

(which yields a positive feedback) is satisfied above some critical temperature, once the lower-tropospheric opacity due to water vapor becomes sufficiently large.

Although the behavior of the longwave radiation feedback term in our channel simulations appears to be consistent with the temperature-dependence suggested by Emanuel *et al.* (2014), cloud effects rather than clear-sky radiative transfer lead to our negative longwave feedback at low T_S (Figure 5). As predicted by Emanuel *et al.* (2014), the clear sky longwave feedback is weaker in the colder simulations – near zero or slightly negative – but this contributes only a small amount to the total longwave feedback. Aggregation occurs in spite of an initially negative longwave feedback at $T_S <= 295$ K, because this negative feedback is overridden by the combination of a positive surface flux and shortwave feedbacks; recall that the increasing strength of the shortwave feedback with decreasing temperature is largely due to clouds.

A negative longwave cloud feedback implies that the atmosphere itself is cooling more in the moist regions and cooling less in the dry regions, due to the presence of clouds. We speculate that this occurs because a low-temperature atmosphere is optically thin, so the addition of clouds can increase the atmospheric longwave cooling by increasing its emissivity. An increase in longwave cooling due to greater cloud fraction in moist regions (where $\widehat{h}' > 0$) is then a negative feedback on aggregation.

A positive shortwave cloud feedback could occur in several ways. More low clouds in the moist regions could increase the reflection of shortwave radiation back into the atmosphere, where it can be absorbed by water vapor, increasing column shortwave heating. More clouds in the moist regions could also directly increase the shortwave heating through shortwave absorption by cloud water, or possibly by increasing atmospheric absorption because of a higher fraction of diffuse radiation. It is unclear why these effects would be stronger at lower temperature.

Taken together, these results indicate that clouds may be of first-order importance in understanding the temperature-dependence of self-aggregation. Negative clear-sky longwave feedbacks at low T_S, as invoked by Emanuel *et al.* (2014), seem insufficient to prevent self-aggregation if surface flux feedbacks and cloud-radiative feedbacks are positive enough. We caution, however, that our cloud-radiative feedbacks may be biased due to the poor representation of low clouds with such coarse resolution.

7.4. *Comparison with Observations*

Observations of the tropical atmosphere over oceans show that area-averaged humidity, outgoing longwave radiation, reflected shortwave radiation, and cloudiness are all reduced as the degree of aggregation increases (Tobin *et al.* 2012, 2013). Some, but not all, of these relationships are also found in our simulations. As described in Section 4, the horizontal mean relative humidity decreases in all our simulations at nearly all heights, and the mean outgoing longwave radiation increases by ∼11-24 W m^{-2}. This is comparable to the increase in observed outgoing longwave radiation of ∼ 20-30 W m^{-2} in more aggregated regimes found by Tobin *et al.* (2013). Observations of aggregated convection, however, find that reflected shortwave radiation is reduced because of reduced total cloud fraction, largely canceling the increase in outgoing longwave radiation (Tobin *et al.* 2012, 2013). This contrasts with simulations in both square and channel geometry, in which aggregation leads to a reduction in high clouds but an increase in low clouds, and the reflected shortwave radiation changes little (Figure 8, Wing (2014)). The difference in cloud liquid and ice concentrations between the beginning and end of the channel simulations implies an increase in cloud optical thickness at low levels and a decrease at middle and high levels. This occurs at all temperatures, but the location of the maximum change in cloud ice moves upward with the tropopause as temperature increases (Figure 8(c)). At a horizontal resolution of 3 km, however, we cannot expect the model to accurately represent low clouds. The response of the surface energy balance also differs between our simulations and observations; we find that aggregation leads to less energy gain by the surface, whereas Tobin *et al.* (2013) found that aggregation leads to more energy gain by the surface. This discrepancy is consistent with the differing responses of low cloud fraction to aggregation, but may also be related to the constraint that we fix T_S, rather than allowing it to evolve freely, as in nature. Our finding of increased domain-mean tropospheric radiative cooling with aggregation agrees with observations, and has contributions from both more longwave cooling and less shortwave heating in a drier troposphere.

7.5. *Sensitivity to Aspect Ratio of Domain*

A limitation of the simulations discussed here is the constrained cross-channel y-dimension. To address this, we run three sensitivity tests at 305 K in which the horizontal aspect ratio (L_x/L_y) of the domain is varied from the default of 64:1 (12288 km $\times$ 192 km), while keeping the horizontal area, number of grid cells, and resolution fixed. These three simulations have aspect ratios L_x/L_y of 16:1 (6144 km $\times$ 384 km), 4:1 (3072 km $\times$ 768 km), and 1:1 (1536 km $\times$ 1536 km). Self-aggregation occurs in each case, taking the form of multiple moist and dry bands in all but the square simulation, in which aggregation manifests as a single, circular cluster (Video S2). The strength of the aggregation increases as the aspect ratio goes from 64:1 to 1:1; less elongated domains experience more domain-mean drying and warming with aggregation, as well as greater spatial variance in precipitable water. The physical mechanisms of aggregation across aspect ratios are similar, with the magnitudes of the diabatic feedbacks in the initial phase of aggregation being nearly identical. The advective term trends from negative to positive in the intermediate stages as the aspect ratio goes from 64:1 to 1:1. This is further evidence that differences in the geometry of dry and moist regions are responsible for differences in the role of advective moist static energy transport. The increasing strength of aggregation as the aspect ratio approaches 1:1 may also be partially caused by these differences in the magnitude and sign of the advective term. The length scale of aggregation is approximately consistent between simulations of different channel length. The 4:1 simulation has 2 bands with $\overline{L_{\{k\}}}^{d50:75} = 1093$ km and the 16:1 simulation has $\sim$5 bands with $\overline{L_{\{k\}}}^{d50:75} = 1368$ km, compared to $\sim$9 bands ($\overline{L_{\{k\}}}^{d50:75} = 1113$ km) in the 64:1 channel. These sensitivity tests support the conclusion that the diabatic mechanisms of self-aggregation are robust across varied domain geometry. They also suggest that the characteristics of self-aggregation, including its length scale, are not unduly influenced by the constrained y-dimension of the channel, at least at 305 K.

8. Summary and Conclusions

In this study, we investigate the behavior of self-aggregation of convection in simulations of non-rotating radiative-convective equilibrium in an elongated 3D channel domain. In these simulations, self-aggregation occurs across a wide range of sea-surface temperatures (T_S = 280 K-310 K), and takes the form of multiple moist and dry bands. We quantify the growth rates, physical mechanisms, and length scales of the aggregation, with the goal of comparing self-aggregation across models and geometries. Using a budget for the spatial variance of frozen moist static energy, we find that diabatic feedbacks dominate the evolution of aggregation in channel geometry; the advective term nearly always damps growth in $\mathrm{var}(\widehat{h})$. These mechanisms are robust to the choice of radiation scheme, although the contribution of clouds is larger with the CAM radiation scheme than with RRTM. A key result is that the behavior of the radiative feedbacks varies with temperature, primarily due to the contribution of clouds. The longwave radiative feedback at the beginning of the simulation becomes negative as T_S is decreased, which is compensated for by an increase in the magnitude of the shortwave radiative feedback.

An advantage of the channel geometry is that the development of multiple convectively active regions permits diagnosis of a characteristic length scale of aggregation, which is a prerequisite to developing a theory for the length scales of self-aggregation. We find that the correlation length of precipitable water grows in time, possibly as a power-law, but upscale growth does not continue past $\mathcal{O}(1000)$ km. As the sea-surface temperature is increased, the aggregated state has more regularity and smaller length scales, although this property is sensitive to the radiation scheme used. Further work is needed to understand why the length scale of aggregation and its scaling with temperature depend on the radiation scheme. We present a theory for the maximum size of a dry region, based on a simple model of remoistening of a well-mixed boundary layer near a subsidence center. The evidence for the relevance of the remoistening length, however, is inconclusive, so the question of what sets the length scale of self-aggregation remains open. In particular, our theory relates to the maximum size of a dry region; does the size of a moist region scale with that of a dry region, or is it controlled by different mechanisms? The occurrence of self-aggregation at low temperatures in channel geometry and its absence at similar temperatures in square geometry hints at a temperature-dependent

minimum length scale, and suggests that self-aggregation may fail to emerge in domains smaller than this minimum scale. We hope that this work inspires further testing of the remoistening length hypothesis, and development of new theories for both minimum and maximum length scales of self-aggregation.

Finally, we compare the changes in humidity, radiative fluxes, and cloudiness that occur with aggregation to the relationships found in observations (e.g., Tobin *et al.* 2013). We find some consistent relationships (for example, between aggregation and humidity and outgoing longwave radiation), but an increase in lower-tropospheric cloud fraction rather than a decrease as in observations. It is unknown whether the changes in cloud fraction with aggregation in our simulations are robust – for example, due to increases in lower-tropospheric stability with aggregation – or an artifact of relatively coarse resolution.

With the exception of the Tobin *et al.* observational studies, research on self-aggregation has been focused on idealized numerical modeling. An important avenue for future work is the relevance of self-aggregation physics to real world phenomena. How does self-aggregation behave in more realistic model configurations, as with background wind shear, or interactive or heterogeneous surface temperatures or subsurface heat export, or including the effects of differential rotation, as on an equatorial beta plane? Do distinct moist and dry modes exist in the real tropical atmosphere, and are they dominantly maintained by differential forcing, diabatic feedbacks, or advection? Using observations to investigate the correlation between anomalies in diabatic forcing and column moisture – while controlling for other influences – would be a critical step towards answering these questions.

Acknowledgements

We acknowledge high-performance computing support from Yellowstone (Computational and Information Systems Laboratory 2012) provided by NCAR's Computational and Information Systems Laboratory, sponsored by the National Science Foundation. Allison A. Wing is supported by an NSF AGS Postdoctoral Research Fellowship, under award No. 1433251. Timothy W. Cronin is supported by a NOAA Climate and Global Change Postdoctoral Fellowship and by the Harvard University Center for the Environment. We thank Marat Khairoutdinov for providing SAM, the cloud resolving model. We also thank Kerry Emanuel, Peter Molnar, Martin Singh, and Adam Sobel for many useful discussions and helpful comments on a draft of the manuscript. We also thank three anonymous reviewers for their thoughtful comments and suggestions for improvement. Both authors contributed equally to this work.

Appendix A: Notation

- Density-weighted vertical integral: $\widehat{A} = \int_0^{z_t} \rho A dz$.
- Horizontal mean: $\langle A \rangle$
- Anomaly from horizontal mean: A'
- Horizontal mean of spatial variance: $\mathrm{var}\,(A)$
- Time mean from day n to day m: $\overline{A}^{dn:m}$
- $y-$averaged precipitable water: $\widehat{q(x)}$
- Power-weighted average wavenumber of spatial variability of precipitable water: $\{k\}$
- Length of long-axis of channel: L_x

Appendix B: Remoistening length theory

To address the question of the upper limit to the size of an anomalously dry region, we develop a simple well-mixed boundary layer model in a non-rotating atmosphere, near the center of a dry region with no convection and uniform subsidence. The model considers the dependence of mixing ratio q, as a function of distance from the subsidence center, under the influence of horizontal advection, vertical advection/entrainment, and surface fluxes (Figure 9). We assume constant boundary layer height z_b and constant subsidence w_f from the free troposphere into the top of the boundary layer. We parameterize moisture exchange between the surface (which has saturation mixing ratio q_s^*) and the boundary layer using a bulk formula, with piston velocity $w_s = c_E u(x)$, where c_E is a dimensionless exchange coefficient $\sim 10^{-3}$. To adequately parameterize surface exchange when resolved winds are weak, we also impose a minimum surface flux wind speed, u^*, so that $w_s = c_E \max(u, u^*)$. In

SAM, u^*=1 m s^{-1}; use of a single fixed minimum wind speed is somewhat artificial, but real turbulent exchange between the surface and atmosphere occurs at scales much smaller than the 3-km horizontal grid used in the model, and some sort of minimum wind speed is common across models. We also assume that the density is constant and the flow is steady in time; under these assumptions, the equation for q becomes:

$$u\frac{\partial q}{\partial x} = \frac{c_E \max(u,u^*)}{z_b}(q_s^* - q) + \frac{w_f}{z_b}(q_f - q). \tag{9}$$

Assuming that $u(0) = 0$, mass flux continuity dictates that $u = w_f x/z_b$. By applying this to (9), canceling terms of w_f/z_b, and then nondimensionalizing, we obtain:

$$\tilde{x}\frac{\partial \tilde{q}}{\partial \tilde{x}} = \max(\tilde{x},\tilde{a})(1-\tilde{q}) + (\tilde{m}-\tilde{q}) \tag{10}$$

$$\tilde{x} = \frac{c_E x}{z_b} \equiv \frac{x}{L_M} \qquad \tilde{a} = \frac{c_E u^*}{w_f} \qquad \tilde{q} = \frac{q}{q_s^*} \qquad \tilde{m} = \frac{q_f}{q_s^*}. \tag{11}$$

Here, $\tilde{x}$ is the nondimensional length, $\tilde{a}$ is the nondimensional length at which the large-scale winds become stronger than the minimum wind speed u^*, $\tilde{q}$ is the nondimensional boundary layer mixing ratio, and $\tilde{m}$ is the nondimensional free-tropospheric mixing ratio. The key length scale is $L_M \equiv z_b/c_E$, which represents a distance over which the boundary layer mixing ratio can be altered significantly by surface fluxes. In the large-$\tilde{x}$ limit, surface fluxes drive the boundary layer towards the sea-surface saturation mixing ratio; the first term on the RHS of (10) dominates. At small $\tilde{x}$, drying due to vertical advection dominates moistening due to surface fluxes, and for very small $\tilde{x} < \tilde{a}$, the resolved winds are too weak to matter at all for the surface fluxes. Even at large $\tilde{x}$, the competition of surface fluxes and vertical advection results in a relaxation to saturation that goes as $\tilde{x}^{-1}$ and not $e^{-\tilde{x}}$ (the latter would occur if vertical advection was neglected). The simplest solution to (10) is given when $u^* = 0$ and thus $\tilde{a} = 0$:

$$\tilde{q} = 1 + (\tilde{m}-1)\frac{1-e^{-\tilde{x}}}{\tilde{x}}. \tag{12}$$

The dashed lines in Figure 10 show this solution for three choices of $\tilde{m}$. Solutions when $\tilde{a} \neq 0$ have a different functional form than (12), and their functional form changes between regions where $\tilde{x} < \tilde{a}$ and $\tilde{x} > \tilde{a}$. The solution in both regions for $\tilde{a} \neq 0$ requires matching $\tilde{q}$ and $d\tilde{q}/d\tilde{x}$ at $\tilde{x} = \tilde{a}$, and is given by:

$$\begin{aligned}
\tilde{q} &= \frac{\tilde{m}+\tilde{a}}{1+\tilde{a}} && : \tilde{x} < \tilde{a} \\
&= 1 + C_1\frac{1-e^{-\tilde{x}}}{\tilde{x}} + \frac{C_2}{\tilde{x}} && : \tilde{x} \geq \tilde{a} \\
C_1 &= \frac{(\tilde{m}-1)e^{\tilde{a}}}{1+\tilde{a}} \\
C_2 &= \frac{(\tilde{m}-1)(\tilde{a}+1-e^{\tilde{a}})}{1+\tilde{a}}.
\end{aligned} \tag{13}$$

The boundary layer mixing ratio is constant for $\tilde{x} < \tilde{a}$, and then smoothly tends towards the earlier solution of (12) for $\tilde{x} \geq \tilde{a}$ (solid lines in Figure 10). Furthermore, if $\tilde{a} = 0$, then C_2 vanishes and (12) is recovered directly from (13) (dashed lines in Figure 10).

This simple boundary layer model of remoistening near a subsidence center can also be used to investigate the influence of geometry of the subsidence region. Rather than assuming that the flow occurs along a channel, we can assume that the flow spreads with circular symmetry, so that the subsidence region is a dry patch rather than a dry band. Imposing cylindrical symmetry weakens the surface flow by a factor of 2 at a given distance from the subsidence center, as compared to the cartesian case, which alters two terms in (10): $\tilde{a}$ becomes $2\tilde{a}$ and $(\tilde{m}-\tilde{q})$ becomes $2(\tilde{m}-\tilde{q})$. These alterations mean that mixing ratio is now constant for $\tilde{x} < 2\tilde{a}$, and that the influence of vertical advection is stronger; the approach to saturation is considerably slower than in the case of Cartesian geometry (dashed-dot line in Figure 10). The solution in cylindrical geometry is algebraically cumbersome but still analytic:

$$\begin{aligned}
\tilde{q}_{\rm cyl} &= \frac{\tilde{m}+\tilde{a}}{1+\tilde{a}} && : \tilde{x} < 2\tilde{a} \\
&= 1 + C_3\frac{1-\tilde{x}-e^{-\tilde{x}}}{\tilde{x}^2} + C_4\left(\frac{1}{\tilde{x}} - \frac{1}{\tilde{x}^2}\right) && : \tilde{x} \geq 2\tilde{a} \\
C_3 &= \frac{2(1-\tilde{m})(1-\tilde{1})e^{2\tilde{a}}}{1+\tilde{a}} \\
C_4 &= \frac{2(1-\tilde{m})e^{2\tilde{a}}}{1+\tilde{a}}\left[2\tilde{a}^2 + (1+\tilde{a})(1-2\tilde{a}-e^{-2\tilde{a}})\right].
\end{aligned} \tag{14}$$

This slower approach to saturation following a parcel out of a dry patch in cylindrical geometry may explain why it has been difficult to simulate more than one moist or dry region in doubly-periodic square domains; remoistening will be slowed, and allowable

length scales of the dry region increased, so long as the dry region occupies less than half of a doubly-periodic square domain, and is thus enclosed by a moist environment.

To test this theory, we run two simulations at 300 K where the neutral moisture exchange coefficient, $c_{E,n}$ is halved and doubled, which results in a rough halving or doubling of c_E, respectively. The doubling and halving of c_E are not exact, because c_E is computed iteratively and depends on the wind speed and stability, both of which change when $c_{E,n}$ is changed. $L_{\{k\}}$ increases to 2586 km (from 1543 km) when $c_{E,n}$ is halved, and decreases to 774 km when $c_{E,n}$ is doubled – changes that are in the right direction and nearly the right magnitude as predicted by the theory if c_E alone changed. But z_b is also altered by varying $c_{E,n}$, increasing to 1643 m (from 850 m) when $c_{E,n}$ is halved, and decreasing to 500 m when $c_{E,n}$ is doubled. Thus, the linear relationship $L_{\{k\}} = 3.16 L_M$ fails to hold when c_E is varied; L_M increases to 1960 km (from 447 km) when $c_{E,n}$ is halved ($L_{\{k\}} = 1.32 L_M$), and decreases to 95 km when $c_{k,n}$ is doubled ($L_{\{k\}} = 8.15 L_M$). This discrepancy might indicate a general weakness of the theory, but it might also lead us to simply infer that the relationship between $L_{\{k\}}$ and L_M depends directly on c_E. This is a reasonable inference because changing c_E directly modifies the only other nondimensional parameter in our theory, $\tilde{a} = c_E u^* / w_f$, which changes the dimensionless solutions for boundary layer mixing ratio evolution. The characteristics of the aggregated state also appear sensitive to c_E, with increased spatial variance of $\mathcal{H}$ when $c_{E,n}$ is halved, and reduced spatial variance of $\mathcal{H}$ when $c_{E,n}$ is doubled. Thus, we do not view these simulations with modified $c_{E,n}$ as particularly strong evidence in support of or opposition to the theory.

Supporting Information

Video S1: This video shows the evolution of aggregation for the 305 K channel simulation. The top subplot shows the cloud-top temperature and the precipitation rate, and the bottom subplot shows the precipitable water. In order to zoom in on the elongated channel, it is divided into quarters and each segment is wrapped left-to-right, as if it were lines of text.

Video S2: This video shows a five day period (days 70-75) from the 305 K simulations at the four different aspect ratios to scale (standard 64:1, 16:1, 4:1, and 1:1). The variables plotted are the same as in Video S1.

References

Abbot D. 2014. Resolved snowball Earth clouds. *J. Climate* **27**: 4391–4402, doi:10.1175/JCLI-D-13-00738.1.

Becker T, Stevens B. 2014. Climate and climate sensitivity to changing CO2 on an idealized land planet. *J. Adv. Model. Earth Sys.* **6**: 1205–1223, doi:10.1002/2014MS000369.

Bray A. 2003. Coarsening dynamics of phase-separating systems. *Philos. Trans. R. Soc. Land. A* **361**: 781–792, doi:10.1098/rsta.2002.1164.

Bretherton CS, Blossey PN, Khairoutdinov M. 2005. An energy-balance analysis of deep convective self-aggregation above uniform SST. *J. Atmos. Sci.* **62**: 4237–4292, doi:10.1175/JAS3614.1.

Clough SA, Shephard MW, Mlawer EJ, Delamere JS, Iacono MJ, Cady-Pereira K, Boukabara S, Brown PD. 2005. Atmospheric radiative transfer modeling: A summary of the AER codes. *J. Quant. Spectrosc. Radiat. Transfer* **91**: 233–244.

Collins WD, Rasch PJ, Boville BA, Hack JJ, McCaa JR, Williamson DL, Briegleb BP, Bitz CM, Lin SJ, Zhang M. 2006. The formulation and atmospheric simulation of the Community Atmosphere Model version 3 (CAM3). *J. Climate* **19**: 2144–2161, doi:10.1175/JCLI3760.1.

Computational, Information Systems Laboratory. 2012. Yellowstone: IBM iDataPlex System (University Community Computing). Boulder, CO: National Center for Atmospheric Research. http://n2t.net/ark:/85065/d7wd3xhc.

Craig GC, Mack JM. 2013. A coarsening model for self-organization of tropical convection. *J. Geophys. Res. Atmos.* **118**: 8761–8769, doi:10.1002/jgrd.50674.

Cronin T. 2014. On the choice of average solar zenith angle. *J. Atmos. Sci.* **71**: 2994–3003, doi:10.1175/AJAS-D-13-0392.1.

Emanuel K, Wing AA, Vincent EM. 2014. Radiative-convective instability. *J. Adv. Model. Earth Syst.* **6**: 75–90, doi:doi:10.1002/2013MS000270.

Grabowski W, Moncrieff M. 2001. Large-scale organization of tropical convection in two-dimensional explicit numerical simulations. *Q. J. R. Meteorol. Soc.* **127**: 445–468.

Grabowski W, Moncrieff M. 2002. Large-scale organization of tropical convection in two-dimensional explicit numerical simulations: Effects of interactive radiation. *Q. J. R. Meteorol. Soc.* **128**: 2349–2375, doi:10.1256/qj.01.104.

Held IM, Hemler RS, Ramaswamy V. 1993. Radiative-convective equilibrium with explicity two-dimensional moist convection. *J. Atmos. Sci* **50**: 3909–3927.

Held IM, Zhao M, Wyman B. 2007. Dynamic radiative-convective equilibria using GCM column physics. *J. Atmos. Sci.* **64**: 228–238, doi:10.1175/JAS3825.11.

Iacono MJ, Delamere JS, Mlawer EJ, Shephard MW, Clough SA, Collins WD. 2008. Radiative forcing by long-lived greenhousegases: calculations with the AER radiative transfer models. *J. Geophys. Res.* **113**: doi:/10.1029/2008JD009944, doi:10.1029/2008JD009944.

Jeevanjee N, Romps DM. 2013. Convective self-aggregation, cold pools, and domain size. *Geophys. Res. Lett.* **40**: doi:10.1002/grl.50204, doi:10.1002/grl/50204.

Khairoutdinov M, Randall D. 2003. Cloud resolving modeling of the ARM Summer 1997 IOP: Model formulation, results, uncertainties, and sensitivities. *J. Atmos. Sci.* **60**: 607–625.

Khairoutdinov MF, Emanuel KA. 2010. Aggregation of convection and the regulation of tropical climate. Preprints. *29th Conference on Hurricanes and Tropical Meteorology* : Tucson, AZ, Amer. Meteorol. Soc.Tucson, AZ, Amer. Meteorol. Soc.

Mlawer EJ, Taubman SJ, Brown PD, Iacono MJ, Clough SA. 1997. Radiative transfer for inhomogeneous atmospheres: RRTM, a validated correlated-k model for the longwave. *J. Geophys. Res.* **102**: 16 663–16 682.

Muller CJ, Held IM. 2012. Detailed investigation of the self-aggregation of convection in cloud resovling simulations. *J. Atmos. Sci.* **69**: 2551–2565, doi:10.1175/JAS-D-11-0257.1.

Nesbitt SW, Zipser EJ, Cecil DJ. 2000. A census of precipitation features in the tropics using TRMM: Radar, ice scattering, and lightning observations. *J. Climate* **13**: 4087–4106.

Nilsson J, Emanuel K. 1999. Equilibrium atmospheres of a two-column radiative-convective model. *Quart. J. R. Meteorol. Soc.* **125**: 2239–2264.

Popke D, Stevens B, Voigt A. 2013. Climate and climate change in a radiative-convective equilibrium version of ECHAM6. *J. Adv. Model. Earth Sys.* **5**: 1–14, doi:10.1029/2012MS000191.

Posselt D, van den Heever S, Stephens G. 2008. Trimodal cloudiness and tropical stable layers in simulations of radiative-convective equilibrium. *Geophys. Res. Lett.* **35**: L08 802, doi:10.1029/2007GL033029.

Posselt D, van den Heever S, Stephens G, Igel M. 2012. Changes in the interaction between tropical convection, radiation, and the large-scale circulation in a warming environment. *J. Climate* **25**: 557–571, doi:10.1175/2011JCLI4167.1.

Raymond D. 2000. The Hadley circulation as a radiative-convective instability. *J. Atmos. Sci.* **57**: 1286–1297.

Reed KA, Medeiros B, Bacmeister JT, Lauritzen PH. 2015. Global radiative-convective equilibrium in the Community Atmosphere Model 5. *J. Atmos. Sci.* doi:10.1175/JAS-D-14-0268.1.

Sessions SL, Sugaya S, Raymond DJ, Sobel AH. 2010. Multiple equilibria in a cloud-resolving model using the weak temperature gradient approximation. *J. Geophys. Res.* **115**, doi:10.1029/2009JD013376.

Singh M, O'Gorman P. 2013. Influence of entrainment on the thermal stratification in simulations of radiative-convective equilibrium. *Geophys. Res. Lett.* **40**: 4398–4403, doi:10.1002/glr.50796.

Sobel A, Maloney E. 2012. An idealized semi-empirical framework for modeling the Madden-Julian Oscillation. *J. Atmos. Sci.* **69**: 1691–1705, doi:10.1175/JAS-D-11-0118.1.

Sobel A, Nilsson J, Polvani L. 2001. The weak temperature gradient approximation and balanced tropical moisture waves. *J. Atmos. Sci.* **58**: 3650–3665.

Sobel AH, Bellon G, Bacmeister J. 2007. Multiple equilibria in a single-column model of the tropical atmosphere. *Geophys. Res. Lett.* **34**: L22 804, doi:10.1029/2007GL031320.

Stephens GL, van den Heever S, Pakula L. 2008. Radiative-convective feedbacks in idealized states of radiative-convective equilibrium. *J. Atmos. Sci.* **65**: 3899–3916, doi:10.1175/2008JAS2524.1.

Su H, Bretherton CS, Chen SS. 2000. Self-aggregation and large-scale control of tropical deep convection: a modeling study. *J. Atmos. Sci.* **57**: 1797–1816.

Takahashi K. 2009. Radiative constraints on the hydrological cycle in an idealized radiative-convective equilibrium model. *J. Atmos. Sci.* **66**: 77–91, doi:10.1175/2008JAS2797.1.

Tan J, Jakob C, Lane TP. 2013. On the identification of the lare-scale properties of tropical convection using cloud regimes. *J. Climate* **25**: 6618–6632, doi:10.1175/JCLI-D-12-00624-1.

Tan J, Jakob C, Rossow WB, Tselioudis G. 2015. Increases in tropical rainfall driven by changes in frequency of organized deep convection. *Nature* **519**: 451–454, doi:10.1038/nature14339.

Tobin I, Bony S, Holloway CE, Grandpeix JY, Seze G, Coppin D, Woolnough SJ, Roca R. 2013. Does convective aggregation need to be represented in cumulus parameterizations? *J. Adv. Model. Earth Syst.* **5**, doi:10.1002/jame.20047.

Tobin I, Bony S, Roca R. 2012. Observational evidence for relationships between the degree of aggregation of deep convection, water vapor, surface fluxes, and radiation. *J. Climate* **25**: 6885–6904.

Tompkins A, Craig G. 1998. Radiative-convective equilibrium in a three-dimensional cloud-ensemble model. *Q. J. R. Meteorol. Soc.* **124**: 2073–2097.

Wing AA. 2014. Physical mechanisms controlling self-aggregation of convection in idealized numerica modeling simulations : MIT Ph.D. Thesis, 146 pp.

Wing AA, Emanuel KA. 2014. Physical mechanisms controlling self-aggregation of convection in idealized numerical modeling simulations. *J. Adv. Model. Earth Syst.* **6**: 59–74, doi:10.1002/2013MS000269.

Yoden S, Bui HH, Nishimoto E. 2014. A minimal model of QBO-like oscillation in a stratosphere-troposphere coupled system under a radiative-moist convective quasi-equilibrium state. *SOLA* **10**: 112–116, doi:10.2151/sola.2014-023.

Table 1. Summary of simulations at different sea-surface temperatures (T_S). See Appendix A for notation conventions and main text for definition of variables; OLR is outgoing longwave radiation, SW_{TOA} is the net shortwave flux at the top of the atmosphere, P is the surface precipitation rate, CWP is the total cloud water path (liquid plus ice condensate), and τ_1 and τ_2 are growth time scales derived from logistic fits to var($\widehat{h}$) and var($\mathcal{H}$), respectively.

		T_S (K)						
variable	units	280	285	290	295	300	305	310
$\overline{\langle OLR \rangle}^{d2:4}$	W m^{-2}	216.2	225.7	236.1	244.4	250.9	257.7	264.9
$\overline{\langle OLR \rangle}^{d50:75}$	W m^{-2}	227.3	236.1	247.9	262.7	269.7	277.3	289.3
$\overline{\langle SW_{TOA} \rangle}^{d50:75}$	W m^{-2}	345.4	344.4	348.8	350.1	347.1	347.1	352.2
$\overline{\langle \mathcal{H} \rangle}^{d2:4}$	-	0.713	0.718	0.713	0.710	0.718	0.742	0.749
$\overline{\langle \mathcal{H} \rangle}^{d50:75}$	-	0.619	0.640	0.622	0.581	0.593	0.581	0.524
$\overline{\mathrm{var}\,(\mathcal{H})}^{d50:75}$	-	0.0197	0.0151	0.0207	0.0266	0.0184	0.0168	0.0195
$\overline{\langle \widehat{q} \rangle}^{d50:75}$	mm	6.10	9.92	14.69	21.59	33.75	52.27	79.05
$\overline{\langle P \rangle}^{d50:75}$	mm d^{-1}	1.64	2.08	2.42	3.03	3.68	4.37	5.37
$\overline{\langle \mathrm{CWP} \rangle}^{d50:75}$	g m^{-2}	62.7	69.8	64.8	65.8	74.4	75.9	71.6
$\overline{5.26 L_{cor}}^{d50:75}$	km	4263	4483	1648	1831	1786	1209	1078
$\overline{L_{\{k\}}}^{d50:75}$	km	2252	2070	1414	1626	1543	1113	1027
τ_1	d	2.38	2.89	3.19	7.50	5.67	5.56	4.67
τ_2	d	1.94	2.63	2.95	5.96	4.97	5.77	4.18
$\overline{\langle z_b \rangle}^{d50:75}$	m	1110	1170	1090	990	850	710	570
$\overline{\langle c_E \rangle}^{d50:75}$	-	1.73e-3	1.81e-3	1.89e-3	1.95e-3	1.90e-3	1.94e-3	1.94e-3

Table 2. Clear-sky percentage contributions to radiative feedbacks. (Second column) Fractional contribution of the clear-sky shortwave feedback from days 60-75; (Third Column) fractional contribution of the clear-sky longwave feedback in the driest 10% of domain over the range of days in column four. 'c' subscript denotes clear sky terms.

T_S (K)	$\overline{\langle \widehat{h}' N'_{Sc} \rangle / \langle \widehat{h}' N'_S \rangle}^{d60:75}$	$\overline{\langle \widehat{h}' N'_{Lc} \rangle_{10\%} / \langle \widehat{h}' N'_L \rangle_{10\%}}^{d}$	days for LW mean
280	29%	86%	d3:8
285	34%	49%	d5:11
290	54%	31%	d4:11
295	62%	41%	d3:11
300	63%	24%	d2:11
305	70%	24%	d2:11
310	79%	33%	d2:11

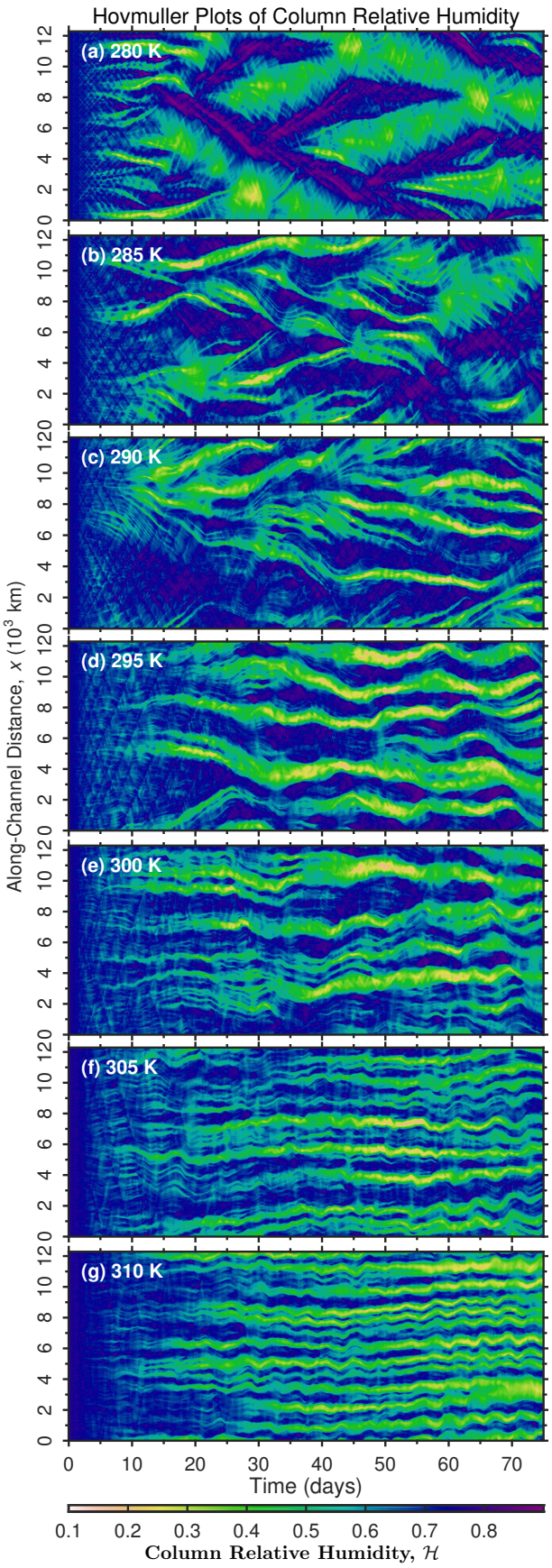

Figure 1. Hovmuller plot of column relative humidity, $\mathcal{H}$ (Equation 1), across the main set of simulations. Time runs left to right, and data are averaged over the short cross-channel y-dimension. Subfigures (a)-(g) are for values of T_S from 280-310 K, in increments of 5 K, with temperature increasing downwards.

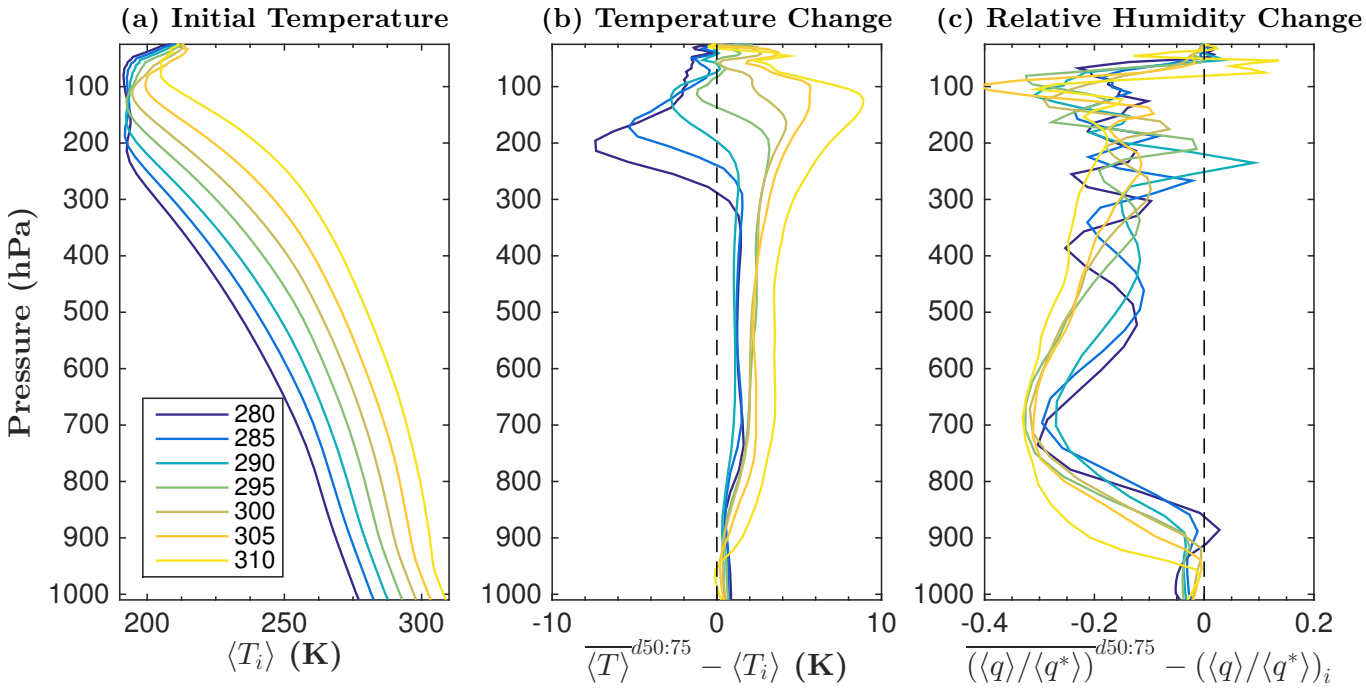

Figure 2. Domain average profiles of (a) initial temperature, and changes between the initial sounding and days 50-75 of each simulation for (b) temperature and (c) relative humidity. Colors indicate sea-surface temperature of the channel simulation, and $\langle \cdot \rangle$ indicates the horizontal mean of a quantity.

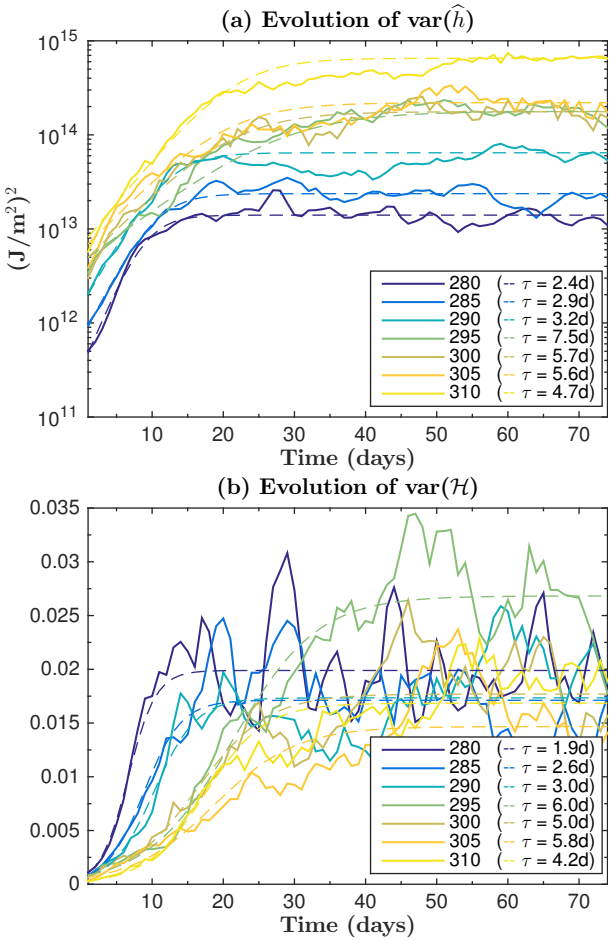

Figure 3. Evolution of (a): var($\widehat{h}$) ($\mathrm{J^2/m^4}$) and (b): var($\mathcal{H}$), in solid lines, and logistic fits to each, in thin dashed lines, for the main set of simulations at different values of T_S. The vertical scale is (a) logarithmic, and (b) linear, and the legend indicates the initial e-folding growth time scale from each logistic fit.

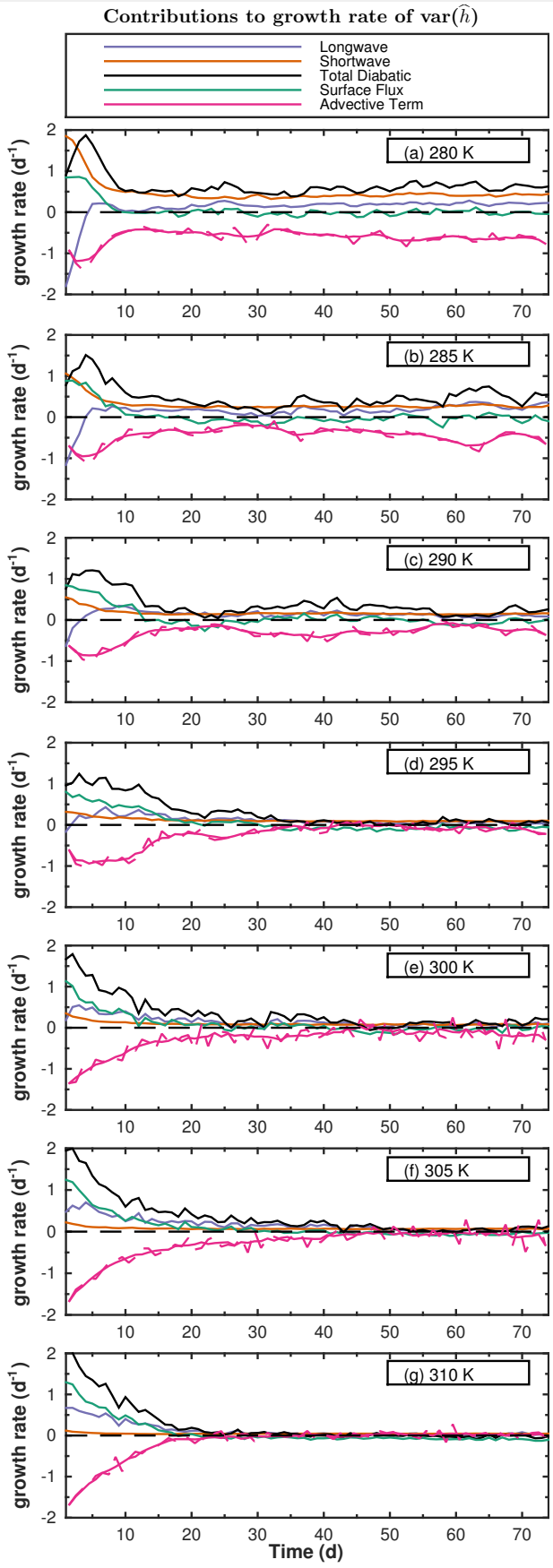

Figure 4. Contributions to growth rate of var$\left(\widehat{h}\right)$, normalized by var$\left(\widehat{h}\right)$ (the terms on the right hand side of Equation (4)), for the the main set of simulations. Shown are the contributions from the (blue) column longwave flux convergence, (red) column shortwave flux convergence, (green) surface enthalpy flux, (pink dashed) horizontal convergence of the column integrated flux of $\widehat{h}$, and (pink) a 5-day running average of the horizontal convergence contribution. The black solid line is the sum of all the diabatic contributions, and the zero line is shown with black dashes. Vertical scales are the same in each panel.

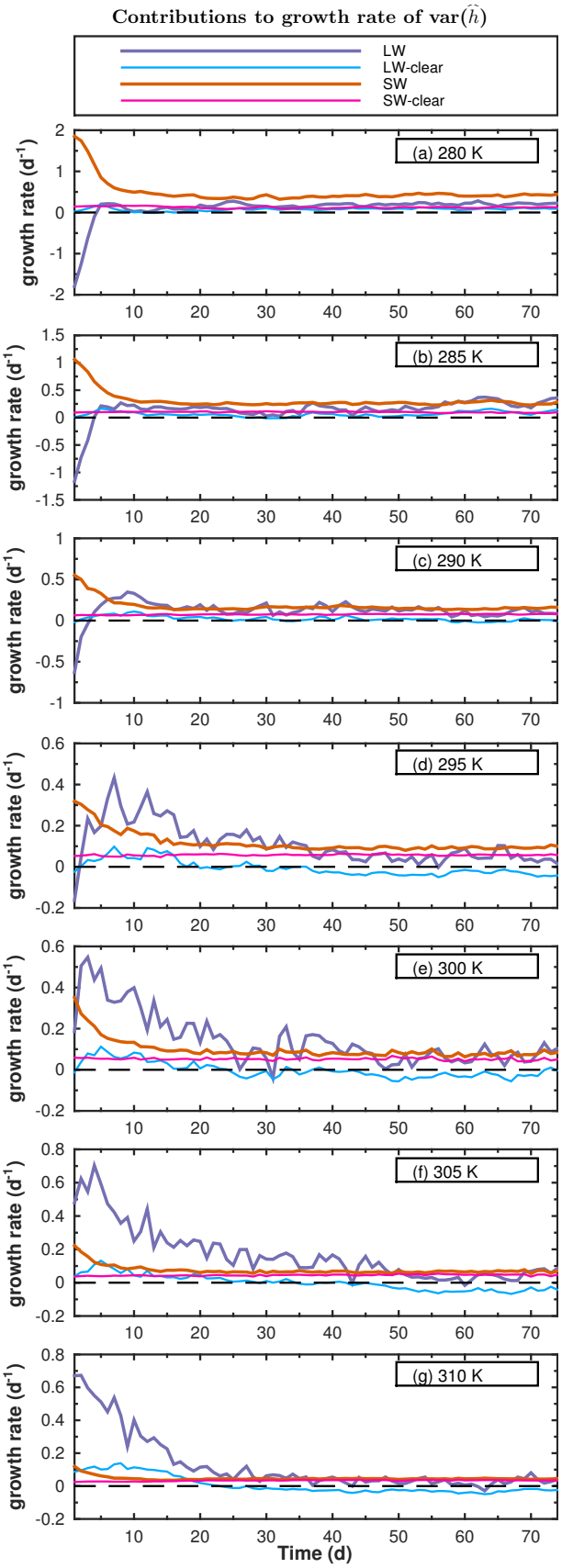

Figure 5. Radiative contributions to growth rate of var$\left(\hat{h}\right)$, normalized by var$\left(\hat{h}\right)$ (the second and third terms on the right hand side of Equation (4)), for the main set of simulations. Shown are the contributions from the (thick blue) column longwave flux convergence, (thin bright blue) clear sky column longwave flux convergence, (thick red) column shortwave flux convergence, and (thin bright red) clear sky column shortwave flux convergence. The zero line is shown with black dashes. Vertical scales are *different* in each panel.

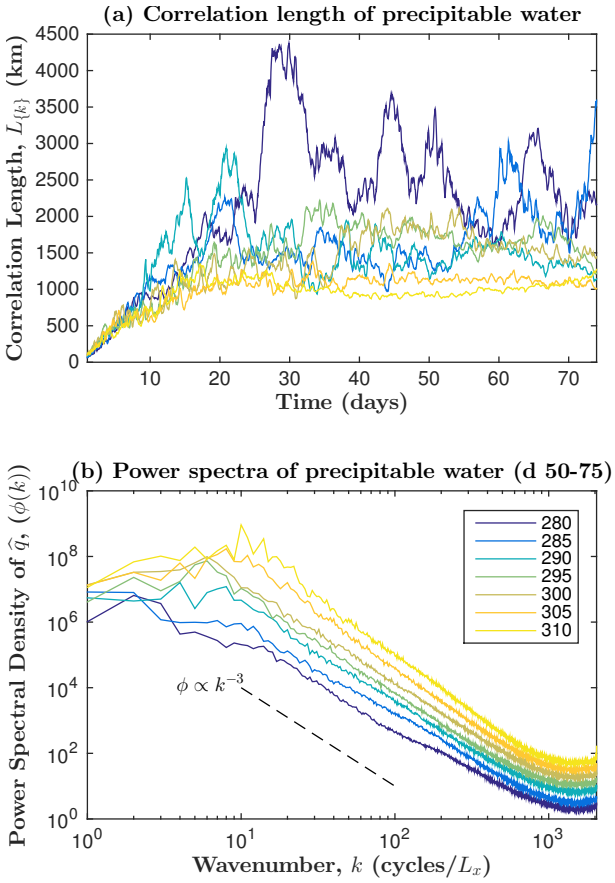

Figure 6. In (a), the evolution of correlation length of precipitable water (PW), using the metric $L_{\{k\}}$, for the main set of simulations. Averages over days 50-75 are given in Table 1. In (b), the power spectra of PW, averaged over days 50-75; the black dashed line indicates the slope of a k^{-3} spectrum.

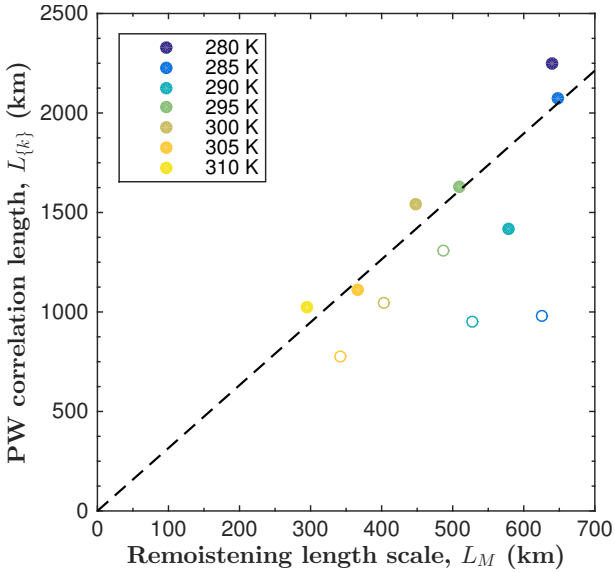

Figure 7. Precipitable water (PW) correlation length, $L_{\{k\}}$, and remoistening length scale $L_M = z_b/c_E$, diagnosed from the main set of simulations (filled circles), and from a set of simulations with an alternative radiation scheme (RRTM, open circles) at different sea-surface temperatures (different colors). The values are from averages over the final 25 days of each simulation. The boundary layer height z_b is calculated as the lower-tropospheric maximum of a three-point quadratic fit of $\partial^2\theta_v/\partial z^2$ in the unsaturated environment, and c_E is the moisture exchange coefficient from Table 1. The dashed line shows the best-fit line through the filled circles and the origin, given by $L_{\{k\}} = 3.16L_M$; the correlation coefficient for this fit is R^2=0.8.

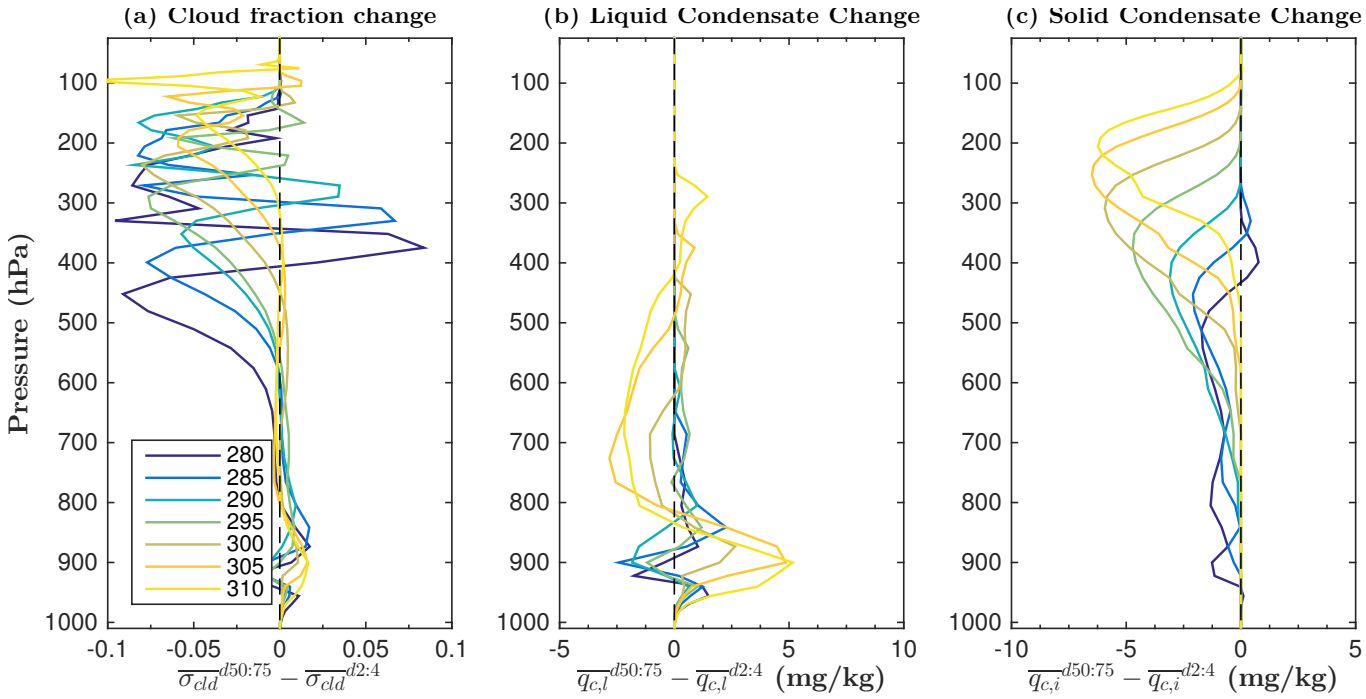

Figure 8. Domain average profiles of change in (a) cloud fraction, (b) liquid condensate $q_{c,l}$ (c) and solid condensate $q_{c,i}$, between days 2-4 and days 50-75. Colors indicate sea-surface temperature of the channel simulation, and an overbar indicates a mean over the time range indicated.

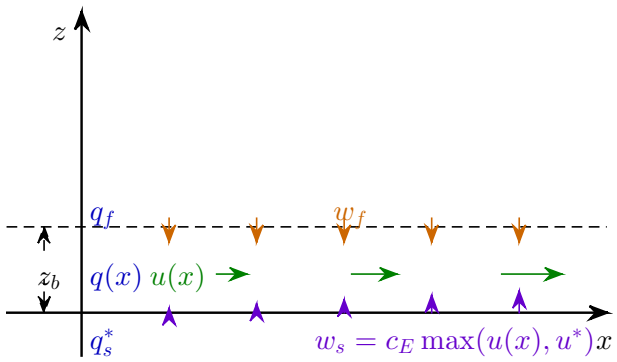

Figure 9. Schematic of boundary layer model for evolution of boundary layer mixing ratio near the center of a subsidence region. See Appendix B for details.

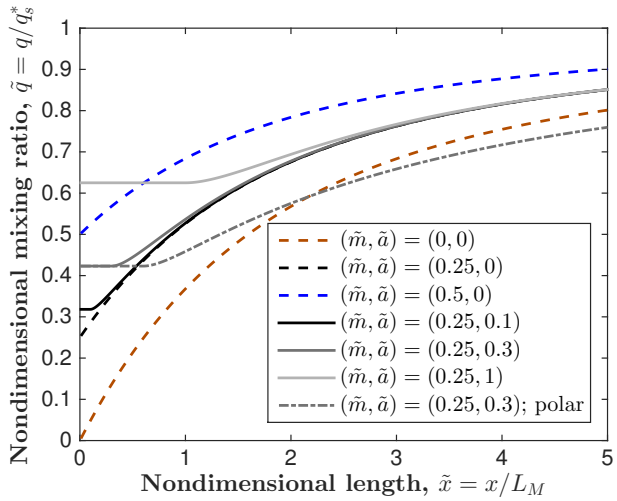

Figure 10. Nondimensional mixing ratio plotted as a function of nondimensional length for the idealized slab boundary layer model, based on (12), (13), and (14).

